
1 **An improved regional coupled modeling system for Arctic sea ice simulation and**
2 **prediction: a case study for 2018**

3

4 **Chao-Yuan Yang¹, Jiping Liu², Dake Chen¹**

5

6 ¹School of Atmospheric Sciences, Sun Yat-sen University, and Southern Marine Science and
7 Engineering Guangdong Laboratory (Zhuhai), Zhuhai, Guangdong, China

8 ²Department of Atmospheric and Environmental Sciences, University at Albany, State
9 University of New York, Albany, NY, USA

10

11 Corresponding author:

12 Chao-Yuan Yang (yangchy36@mail.sysu.edu.cn) and Jiping Liu (jliu26@albany.edu)

13

14

15 **Abstract**

16 The improved/updated Coupled Arctic Prediction System (CAPS) is evaluated by a set of
17 Pan-Arctic prediction experiments for the year 2018, which is built on Weather Research and
18 Forecasting model (WRF), the Regional Ocean Modeling System (ROMS), the Community
19 Ice Code (CICE), and a data assimilation based on the Local Error Subspace Transform
20 Kalman Filter. We analyze physical process linking improved/changed physical
21 parameterizations in WRF, ROMS, and CICE to changes in the simulated Arctic sea ice state.
22 Our results show that the improved convection and boundary layer schemes in WRF result in
23 improved simulation in downward radiative fluxes and near surface air temperature, which
24 influences the predicted ice thickness. The changed tracer advection and vertical mixing
25 schemes in ROMS reduces the bias in sea surface temperature and changes ocean temperature
26 and salinity structure in the surface layer, leading to improved evolution of the predicted ice
27 extent (particularly correcting the late ice recovery issue in the previous CAPS). The improved
28 sea ice thermodynamics in CICE have noticeable influences on the predicted ice thickness. The
29 updated CAPS can better predict the evolution of Arctic sea ice during the melting season
30 compared with its predecessor, though the prediction still have some biases at the regional scale.
31 We further show that the updated CAPS can remain skillful beyond the melting season, which
32 may have potential values for stakeholders making decisions for socioeconomical activities in
33 the Arctic.

34

35

36 1. Introduction

37 Over the past few decades, the extent of Arctic sea ice has decreased rapidly and entered
38 a thinner/younger regime associated with global climate change (e.g., Kwok, 2018; Serreze
39 and Meier, 2019). The dramatic changes in the properties of Arctic sea ice have gained
40 increasing attentions by a wide range of stakeholders, such as trans-Arctic shipping, natural
41 resource exploration, and activities of coastal communities relying on sea ice (e.g., Newton et
42 al., 2016). This leads to increasing demands on skillful Arctic sea ice prediction, particularly at
43 seasonal timescale (e.g., Jung et al., 2016; Liu et al., 2019; Stroeve et al., 2014). However,
44 Arctic sea ice prediction based on different approaches (e.g., statistical method and dynamical
45 model) submitted to the Sea Ice Outlook, a community effort managed by the Sea Ice Prediction
46 Network (SPIN, <https://www.arcus.org/sipn>), shows substantial biases in the predicted seasonal
47 minimum of Arctic sea ice extent compared to the observations for most years since 2008 (Liu
48 et al., 2019; Stroeve et al., 2014).

49 Recently, we have developed an atmosphere-ocean-sea ice regional coupled modeling
50 system, for seasonal Arctic sea ice and climate prediction (Yang et al., 2020, hereafter Y20), in
51 which the Los Alamos Sea Ice Model (CICE) is coupled with the Weather Research and
52 Forecasting Model (WRF) and the Regional Ocean Modeling System (ROMS), hereafter called
53 Coupled Arctic Prediction System (CAPS). To improve the accuracy of initial sea ice
54 conditions, CAPS employs an ensemble-based data assimilation system to assimilate satellite-
55 based sea ice observations. Seasonal Pan-Arctic sea ice predictions with improved initial sea
56 ice conditions conducted in Y20 have shown that CAPS has the potential to provide skillful

57 Arctic sea ice prediction at seasonal timescale.

58 We know that the changes of sea ice variables (e.g., ice extent, ice concentration, ice
59 thickness, ice drift) are mainly driven by forcings from the atmosphere and the ocean.
60 Atmospheric cloudiness and related radiation influence surface ice melting (Huang et al., 2019;
61 Kapsch et al., 2016; Kay et al., 2008) and the energy stored in the surface mixed layer that
62 determines the seasonal ice melt and growth (e.g., Perovich et al., 2011, 2014). Atmospheric
63 circulation is the primary driver for the transportation of sea ice and partly responsible for the
64 variability of Arctic sea ice (e.g., Mallett et al., 2021; Ogi et al., 2010; Zhang et al., 2008).
65 Olonscheck et al. (2019) suggested that atmospheric temperature fluctuations explain a
66 majority of Arctic sea ice variability while other drivers (e.g., surface winds, and poleward heat
67 transport) account for about 25% of Arctic sea ice variability. The oceanic heat inputs (as well
68 as salt inputs) into the Arctic Ocean include the Atlantic Water (AW; Aagaard, 1989;
69 McLaughlin et al., 2009) through the Barents Sea, and the Pacific Water (PW; Itoh et al., 2013;
70 Woodgate et al., 2005) from the Bering Strait. The oceanic heat inputs from AW and PW are
71 not directly available for sea ice since they are separated from a cold and fresh layer underlying
72 sea ice (e.g., Carmack et al., 2015, Fig. 2). Vertical mixing by the internal wave (e.g., Fer, 2014)
73 and double diffusion (e.g., Padman and Dillon, 1987; Turner, 1973) are the principal processes
74 for upward heat transport from the subsurface layer (i.e., AW and PW) to the surface mixed
75 layer in the Arctic Ocean. Sea ice thermodynamics determines how thermal properties of sea
76 ice (e.g., temperature, salinity) change. These changes then influence the thermal structure of
77 underlying ocean through interfacial fluxes (i.e., heat, salt and freshwater fluxes; DuVivier et

78 al., 2021; Kirkman IV and Bitz, 2011) and ice thickness (e.g., Bailey et al., 2020).

79 The CAPS is configured for the Arctic with sufficient flexibility. That means each model
80 component of CAPS (WRF, ROMS, and CICE) has different physics options for us to choose
81 and capability to integrate ongoing improvements in physical parameterizations. Recently, the
82 WRF model has adapted improved convection and boundary layer schemes in the Rapid
83 Refresh (RAP) model operational at the National Centers for Environmental Prediction (NCEP,
84 Benjamin et al., 2016). The first question we want to answer in this paper is to what extent
85 these modifications can improve atmospheric simulations in the Arctic (i.e., radiation,
86 temperature, humidity, and wind), and then benefit seasonal Arctic sea ice simulation and
87 prediction. The ROMS model provides several options for tracer advection schemes. These
88 advection schemes can have different degrees of oscillatory behavior (e.g., Shchepetkin and
89 McWilliams, 1998). The oscillatory behavior can have impacts on sea ice simulation through
90 ice-ocean interactions (e.g., Naughten et al., 2017). The second question we want to answer in
91 this paper is to what extent different advection schemes can change the simulation of upper
92 ocean thermal structure and then Arctic sea ice prediction. Several recent efforts have
93 incorporated prognostic salinity into sea ice models. The CICE model has a new mushy-layer
94 thermodynamics parameterization that includes prognostic salinity and treats sea ice as a two-
95 phase mushy layer (Turner et al., 2013). Bailey et al. (2020) showed that the mushy-layer
96 physics has noticeable impacts on Arctic sea ice simulation within the Community Earth
97 System Model version 2. The third question we want to answer in this paper is whether the
98 mushy-layer scheme can produce noticeable influence on seasonal Arctic sea ice prediction.

99 Currently, SIPN focuses on Arctic sea ice predictions during the melting season, particularly
100 seasonal minimum. It is not clear that how predictive skills of dynamical models participating
101 in SIPN may change for longer period, i.e., extending into the freezing up period, which also
102 have significance on socioeconomic aspects. The assessment of the skills of global climate
103 models (GCMs) in predicting Pan-Arctic sea ice extent with suites of hindcasts suggested that
104 GCMs may have skill at lead times of 1-6 months (e.g., Blanchard-Wrigglesworth et al., 2015;
105 Chevallier et al., 2013; Guemas et al., 2016; Merryfield et al., 2013; Msadek et al., 2014;
106 Peterson et al., 2015; Sigmond et al., 2013; Wang et al., 2013; Zampieri et al., 2018). Moreover,
107 some studies using a “perfect model” approach, which treats one member of an ensemble as
108 the truth (i.e., assuming the model is perfect without bias) and analyzes the skill of other
109 members in predicting the response of the “truth” member (e.g., Meehl et al., 2007), suggested
110 that Arctic sea ice cover can be potentially predictable up to two years in advance (e.g.,
111 Blanchard-Wrigglesworth et al., 2011; Blanchard-Wrigglesworth and Bushuk, 2018; Day et al.,
112 2016; Germe et al., 2014; Tietsche et al., 2014). The last question we want to answer in this
113 paper is whether CAPS has predictive skill for longer periods (up to 7 months).

114 This paper is structured as follows. Section 2 provides a brief overview of CAPS,
115 including model configurations and data assimilation procedures. Section 3 describes the
116 designs of the prediction experiments for the year of 2018 based on major improvements/
117 changes in the model components compared to its predecessor described in Y20, examines the
118 performance of the updated CAPS, and offers physical links between Arctic sea ice changes
119 and improved/changed physical parameterizations. Section 4 discusses the predictive skill of

120 CAPS at longer timescale. Discussions and concluding remarks are given in section 5.

121 **2. Coupled Arctic Prediction System (CAPS)**

122 As described in Y20, the CAPS has been developed by coupling the Community Ice Code
123 (CICE) with the Weather Research and Forecasting Model (WRF) and the Regional Ocean
124 Modeling System (ROMS) based on the framework of the Coupled Ocean-Atmosphere-Wave-
125 Sediment Transport (Warner et al., 2010). The general description of each model component in
126 CAPS is referred to Y20. The advantage of CAPS is its model components have a variety of
127 physics for us to choose and capability to integrate follow-up improvements of physical
128 parameterizations. With recent achievements of community efforts, we update CAPS based on
129 newly-released WRF, ROMS, and CICE models. During this update, we focus on the Rapid
130 Refresh (RAP) physics in the WRF model, the oceanic tracer advection scheme in the ROMS
131 model, sea ice thermodynamics in the CICE model (see details in section 3), and investigate
132 physical process linking them to Arctic sea ice simulation and prediction. The same physical
133 parameterizations described in Y20 are used here for the control simulation (see Table 1). Major
134 changes in physical parameterizations as well as the model infrastructure in the WRF, ROMS,
135 and CICE models are described in section 3.

136 As described in Y20, the Parallel Data Assimilation Framework (PDAF, Nerger and Hiller,
137 2013) was implemented in CAPS, which provides a variety of optimized ensemble-based
138 Kalman filters. The Local Error Subspace Transform Kalman Filter (LESTKF; Nerger et al.,
139 2012) is used to assimilate satellite-observed sea ice parameters. The LESTKF projects the
140 ensemble onto the error subspace and then directly computes the ensemble transformation in

141 the error subspace. This results in better assimilation performance and higher computational
142 efficiency compared to the other filters as discussed in Nerger et al. (2012).

143 The initial ensembles are generated by applying the second-order exact sampling (Pham,
144 2001) to simulated sea ice state vectors (ice concentration and thickness) from an one-month
145 free run, and then assimilating sea ice observations, including: 1) the near real-time daily Arctic
146 sea ice concentration processed by the National Aeronautics and Space Administration (NASA)
147 Team algorithm (Maslanik and Stroeve, 1999) obtained from the NSIDC
148 (<https://nsidc.org/data/NSIDC-0081/>), and 2) a combined monthly sea ice thickness derived
149 from the CryoSat-2 (Laxon et al., 2013; obtained from <http://data.seaiceportal.de>), and daily
150 sea ice thickness derived from the Soil Moisture and Ocean Salinity (SMOS; Kaleschke et al.,
151 2012; Tian-Kunze et al., 2014; obtained from [https://icdc.cen.uni-hamburg.de/en/l3c-smos-](https://icdc.cen.uni-hamburg.de/en/l3c-smos-sit.html)
152 [sit.html](https://icdc.cen.uni-hamburg.de/en/l3c-smos-sit.html)). To address the issue that sea ice thickness derived from CyroSat-2 and SMOS are
153 unavailable during the melting season, the melting season ice thickness is estimated based on
154 the seasonal cycle of the Pan-Arctic Ice Ocean Modeling and Assimilation System (PIOMAS)
155 daily sea ice thickness (Zhang and Rothrock, 2003).

156 Different from Y20, in this study, we change the localization radius from 2 to 6 grids
157 during the assimilation procedures to reduce some instability during initial Arctic sea ice
158 simulations associated with 2 localization radii. As shown in Supplementary Figure S1, the ice
159 thickness with 2 localization radii and 1.5 m uncertainty (used in Y20) shows some
160 discontinuous features (Fig. S1a), which tends to result in numerical instability during the
161 initial integration. Such discontinuous features are obviously corrected with 6 localization radii

162 and 0.75 m uncertainty (Fig. S1b). Following Y20, here we test the 2018 prediction experiment
163 with 6 localization radii for the data assimilation, which shows very similar temporal evolution
164 of the total Arctic sea ice extent for the July experiment relative to that of Y20, although it (red
165 solid line) predicts slightly less ice extent than that of Y20 (blue line) (Supplementary Figure
166 S2). In this study, this configuration is designated as the reference for the following assessment
167 of the updated CAPS (hereafter Y20_MOD).

168 For the evaluation of Arctic sea ice prediction, Sea Ice Index (Fetterer et al., 2017;
169 obtained from <https://nsidc.org/data/G02135>) is used as the observed total sea ice extent, and
170 the NSIDC sea ice concentrations (SIC) derived from Special Sensor Microwave
171 Imager/Sounder (SSMIS) with the NASA Team algorithm (Cavalieri et al., 1996; obtained from
172 <https://nsidc.org/data/nsidc-0051>) is also used. For the assessment of the simulated atmospheric
173 and oceanic variables, the ECMWF reanalysis version 5 (ERA5; Hersbach et al., 2020;
174 obtained from <https://cds.climate.copernicus.eu>) and National Oceanic and Atmospheric
175 Administration (NOAA) Optimum Interpolation (OI) Sea Surface Temperature (SST)
176 (Reynolds et al., 2007; obtained from
177 <https://psl.noaa.gov/data/gridded/data.noaa.oisst.v2.highres.html>) are utilized. For the
178 comparison of spatial distribution, SIC, ERA5, and OISST are interpolated to the model grid.

179 **3. Evaluation of updated CAPS**

180 **3.1. Experiment designs and methodology**

181 The model domain includes 319 (449) x- (y-) grid points with a ~24 km grid spacing for
182 all model components (see Figure 2 in Y20). The WRF model uses 50 vertical levels, the

183 ROMS model uses 40 vertical levels, and the CICE model uses 7 ice layers, 1 snow layer, and
184 5 categories of sea ice thickness. The coupling frequency across all model components is 30
185 minutes. Initial and boundary conditions for the WRF and ROMS models are generated from
186 the Climate Forecast System version 2 (CFSv2, Saha et al., 2014) operational forecast archived
187 at NCEP (<http://nomads.ncep.noaa.gov/pub/data/nccf/com/cfs/prod/>). Sea ice initial conditions
188 are generated from the data assimilation described in section 2. Ensemble predictions with 8
189 members are conducted. A set of numerical experiments for the Pan-Arctic seasonal sea ice
190 prediction with different physics, starting from July 1st to October 1st for the year of 2018, has
191 been conducted. Table 2 provides the details of these experiments that allow us to examine
192 physical process linking improved/changed physical parameterizations in the updated CAPS
193 to Arctic sea ice simulation and prediction.

194 In this study, sea ice extent is calculated as the sum of area of all grid cells with ice
195 concentration greater than 15%. Besides the total Arctic sea ice extent, we also calculate the
196 ice extent for the following subregions: 1) Beaufort and Chukchi Seas (120°W-180, 60°N-
197 80°N), 2) East Siberian and Laptev Seas (90°E-180, 60°N-80°N), and 3) Barents, Kara, and
198 Greenland Seas (30°W-90°E, 60°N-80°N). To further assess the predictive skill of Arctic sea
199 ice predictions, we show the climatology prediction (CLIM, the period of 1998-2017) and the
200 damped anomaly persistence prediction (DAMP). Following Van den Dool (2006), the DAMP
201 is generated from the initial sea ice extent anomaly (relative to the 1998-2017 climatology)
202 scaled by the autocorrelation and the ratio of standard deviation between different lead times
203 and initial times (see the DAMP equation in Y20).

204 In order to understand physical contributors that drive the evolving Arctic sea ice state,
205 the mass budget of Arctic sea ice for all experiments is analyzed in this study as defined in
206 Notz et al. (2016, Append. E), including 1) sea ice growth in supercooled open water (frazil ice
207 formation), 2) basal growth, 3) snow-to-ice conversion, 4) top melt, 5) basal melt, 6) lateral
208 melt, and 7) dynamics process.

209 **3.2. Impacts of the RAP physics in the WRF model**

210 To examine the performance of the upgrades of physical parameterization in component
211 models in CAPS one step at a time compared to its predecessor in Y20, we define the
212 Y21_CTRL experiment that uses the RAP physics in the WRF model (see Table 2 for
213 differences between Y21_CTRL and Y20_MOD). Recently, the Rapid Refresh (RAP) model,
214 a high-frequency weather prediction/assimilation modeling system operational at the National
215 Centers for Environmental Prediction (NCEP), has made some improvements in the WRF
216 model physics (Benjamin et al., 2016), including improved Grell-Freitas convection scheme
217 (GF) and Mellor-Yamada-Nakanishi-Niino planetary boundary layer scheme (MYNN). For the
218 GF scheme, the major improvements relative to the original scheme (Grell and Freitas, 2014)
219 include: 1) a beta probability density function used as the normalized mass flux profile for
220 representing height-dependent entrainment/detrainment rates within statistical-averaged deep
221 convective plumes, which is given as:

$$224 \quad Z_{u,d}(r_k) = cr_k^\alpha - (1 - r_k)^\beta - 1$$

222 where $Z_{u,d}$ is the mass flux profiles for updrafts and downdrafts, c is a normalization constant,
223 r_k is the location of the mass flux maximum, α and β determine the skewness of the beta

225 probability density function, and 2) the ECMWF approach used for momentum transport due
226 to convection (Biswas et al. 2020; Freitas et al. 2018; 2021). For the MYNN scheme, the RAP
227 model improves the mixing-length formulation, which is designed as:

236
$$\frac{1}{l_m} = \frac{1}{l_s} + \frac{1}{l_t} + \frac{1}{l_b}$$

228 where l_m is the mixing length, l_s is the surface length, l_t is the turbulent length, and l_b is
229 the buoyancy length. Compared to the original scheme, the RAP model changed coefficients
230 in the formulation of l_s , l_t , and l_b for reducing the near-surface turbulent mixing, and the
231 diffusivity of the scheme. The RAP model also removes numerical deficiencies to better
232 represent subgrid-scale cloudiness (Benjamin et al. 2016, see Append. B) compared to the
233 original scheme (Nakanishi and Nino, 2009). In addition, some minor issues in the Noah land
234 surface model (Chen and Dudhia, 2001) have been fixed, including discontinuous behavior for
235 soil ice melting, negative moisture fluxes over glacial, and associated with snow melting.

237 Apparently, the above RAP physics can have influence on the behavior of simulated
238 atmospheric thermodynamics (i.e., radiation, temperature). Figure 1 and 2 show the spatial
239 distribution of the ERA5 surface downward solar and thermal radiation (SWDN and LWDN),
240 the prediction errors (ensemble mean minuses ERA5) of Y20_MOD, and the difference
241 between Y21_CTRL and Y20_MOD. For July, Y20_MOD (Fig. 1d) results in less SWDN over
242 most of ocean basins as well as Alaska and northeast US, western Siberia, and eastern Europe,
243 but more SWDN over southern and eastern Siberia compared with ERA5. For August and
244 September (Fig. 1e-f), the spatial distribution is generally similar to that of July, except that
245 eastern Siberia (less SWDN) and northern Canada (more SWDN) in August. It appears that the

246 magnitude of the prediction errors tends to decrease over the areas with large prediction errors
247 as the prediction time increases (i.e., July vs. September). Compared with Y20_MOD, the RAP
248 physics in Y21_CTRL result in large areas with smaller prediction errors in July (e.g., the
249 positive difference between Y21_CTRL and Y20_MOD reduces the negative prediction errors
250 in Y20_MOD), except the north Pacific (especially the Sea of Okhotsk) and north Canada (Fig.
251 1g). For August and September (Fig. 1h, i), encouragingly, there are more areas with smaller
252 prediction errors.

253 In contrast to SWDN, the prediction errors of LWDN in Y20_MOD has much smaller
254 magnitude (up to 100 W/m² in SWDN vs. 50 W/m² in LWDN) for the entire prediction period
255 (Fig. 2d-f). For July, Y20_MOD (Fig. 2d) simulates less LDWN over most of the model domain
256 compared with ERA5, except the Atlantic sector and north Greenland. For August, the areas
257 with negative prediction errors expand and the magnitude of prediction errors increases
258 (particularly in southeastern Siberia and northeast US) compared to that of July (Fig. 2e). For
259 September (Fig. 2f), the spatial distribution of LWDN is mostly similar to that of July, except
260 that north Canada and Canadian Archipelago show positive prediction errors. The Y21_CTRL
261 experiment with the RAP physics tends to reduce the prediction errors in Y20_MOD, especially
262 over eastern Siberia and the Atlantic sector in July to September (Fig. 2g-i).

263 Figure 3 shows the spatial distribution of the ERA5 2m air temperature, the prediction
264 errors of Y20_MOD, and the difference between Y21_CTRL and Y20_MOD. For Y20_MOD,
265 the predicted air temperature in July has small cold prediction errors over all ocean basins,
266 small-to-moderate cold prediction errors (~3-5 degrees) over Canada and Siberia, and

267 moderate-to-large cold prediction errors (~6-9 degrees) over eastern Europe (Fig. 3d). In
268 August (Fig. 3e), the cold prediction errors over most of the model domain are increased, in
269 particular, very large cold prediction error (over 10 degrees) is located over east Siberia. In
270 September, these cold prediction errors are decreased relatively, and some warm prediction
271 errors are found in north of Greenland (Fig. 3f). With the adaptation of the RAP physics in the
272 WRF model, Y21_CTRL, in general, produces a warmer state in most of the model domain
273 compared to that of Y20_MOD during the entire prediction period. For July (Fig. 3g), the
274 predicted air temperature is slightly warmer over the Arctic Ocean, the Pacific, and Atlantic
275 sectors, moderately warmer (~1-2 degrees) over central and eastern Siberia and Canadian
276 Archipelago, but the slightly colder over northern Canada than that of Y20_MOD. For August
277 and September (Fig. 3h), most of the model domain is warmer in Y21_CTRL than that of
278 Y20_MOD, in particular excessive cold prediction errors shown in Y20_MOD over Siberia are
279 reduced notably (~2.5-4 degrees). We notice that the RAP physics does not have significant
280 impacts on atmospheric circulation, given that Y21_CTRL and Y20_MOD have very similar
281 wind pattern (not shown).

282 Figure 4 shows the temporal evolution of the ensemble mean of the predicted Arctic sea
283 ice extent along with the NSIDC observations. In terms of the total ice extent, compared to the
284 Y20_MOD experiment (blue line), the Y21_CTRL experiment (yellow line) produces ~0.5
285 million km² more ice extent at the initial. Note that the difference in the initial ice extent is
286 related to that sea ice fields in Y20_MOD and Y21_CTRL (as well as other experiments listed
287 in Table 2) are initialized based on one-month free runs (section 2), which use different physical

288 configurations listed in Table 2. These one-month free runs do not have the same evolution in
289 sea ice fields and result in different initial ice fields after data assimilation. The ice extent in
290 Y21_CTRL decreases faster than Y20_MOD during the first 2-week integration. After that,
291 they track each other closely, and predict nearly the same minimum ice extent (~4.3 million
292 km²). Like Y20_MOD, Y21_CTRL still has a delayed ice recovery in late September compared
293 to the observation. Compared with the CLIM/DAMP predictions (black dashed and dotted
294 lines), both Y20_MOD and Y21_CTRL have smaller prediction errors in August, but
295 comparable prediction errors after early September.

296 The difference in sea ice extent becomes larger at regional scales, in the East Siberian-
297 Laptev Seas, Y20_CTRL shows faster ice decline after mid-July than that of Y21_MOD,
298 whereas in the Beaufort-Chukchi Seas, Y21_CTRL predicts slower ice retreat after late July
299 than that of Y20_MOD (Fig. 4a, 4b). They are consistent with that Y21_CTRL predicts warmer
300 (relatively colder) temperature than that of Y20_MOD in the East Siberian-Laptev (Beaufort-
301 Chukchi) Seas. Both Y20_MOD and Y21_CTRL agree well with the observations in the
302 Barents-Kara-Greenland Seas (Fig. 4c). Compared with the observations, Y20_MOD performs
303 relatively better in regional ice extents than that of Y21_CTRL. Figure 5 shows the spatial
304 distribution of the NSIDC sea ice concentration and the difference between the predicted ice
305 concentration and the observations for all grid cells that the predictions and the observations
306 both have at least 15% ice concentration. The vertical and horizontal lining areas represent
307 difference of the ice edge location. Like the regional ice extent shown in Figure 4, Y21_CTRL
308 predicts lower (higher) ice concentration along the East Siberian-Laptev (Beaufort-Chukchi)

309 Seas (Fig. 5e₁-e₃). Y21_CTRL also predicts less ice in the central Arctic Ocean in August and
310 September, which is consistent with warmer temperature in Y21_CTRL relative to Y20_MOD.

311 Figure 6 shows the evolution of sea ice mass budget terms of Y20_MOD and Y21_CTRL,
312 averaged with cell-area weighting over the entire model domain. During the entire prediction
313 period, most of the ice loss in Y20_MOD and Y21_CTRL are caused by basal melting. The
314 surface melting has relatively small contribution in the total ice loss and mainly occurs in July.
315 However, compared with Y20_MOD (Fig. 6a), Y21_CTRL (Fig. 6b) shows much larger
316 magnitude for basal and surface melt. In a fully coupled predictive model, the changes of sea
317 ice are determined by the fluxes from the atmosphere above and the ocean below. Associated
318 with the increased downward radiation of the above RAP physics, Y21_CTRL absorbs more
319 shortwave radiation (SWABS, Fig. 7a) and allows more penetrating solar radiation into the
320 upper ocean below sea ice (SWTHRU, Fig. 7b) than that of Y20_MOD, especially in July. This
321 explains why Y21_CTRL has larger magnitude of surface and basal melting terms. Although
322 Y21_CTRL show larger magnitude in surface and basal melting than that of Y20_MOD, the
323 ice extent in Y21_CTRL and Y20_MOD shown in Figure 4 show similar evolution. The effect
324 of larger surface and basal melting in Y21_CTRL is largely reflected in the ice thickness change.
325 As shown in Figure S3, Y21_CTRL has thinner ice thickness than that of Y20_MOD, in the
326 East Siberian-Laptev Seas in July and in the much of central Arctic Ocean in August and
327 September.

328

329 **3.3. Impacts of the tracer advection in ROMS model**

330 Currently, the ROMS model that uses a generalized topography-following coordinate has
331 two vertical coordinate transformation options:

$$348 \quad z(x, y, \sigma, t) = S(x, y, \sigma) + \zeta(x, y, t) \left[1 + \frac{S(x, y, \sigma)}{h(x, y)} \right] \quad (1)$$
$$S(x, y, \sigma) = h_c \sigma + [h(x, y) - h_c] C(\sigma)$$

332 or

$$349 \quad z(x, y, \sigma, t) = \zeta(x, y, t) + [\zeta(x, y, t) + h(x, y)] S(x, y, \sigma)$$
$$S(x, y, \sigma) = \frac{h_c \sigma + h(x, y) C(\sigma)}{h_c + h(x, y)} \quad (2)$$

333 where $S(x, y, \sigma)$ is a nonlinear vertical transformation function, $\zeta(x, y, t)$ is the free-surface,
334 $h(x, y)$ is the unperturbed water column thickness, $C(\sigma)$ is the non-dimensional, monotonic,
335 vertical stretching function, and h_c controls the behavior of the vertical stretching. In Y20, we
336 used the transformation 1 and the vertical stretching function introduced by Song and
337 Haidvogel (1994). However, the vertical transformation 1 has an inherent limitation for the
338 value of h_c (expected to be the thermocline depth), which must be less than or equal to the
339 minimum value in $h(x, y)$. As a result, h_c was chosen as 10 meters due to the limitation of
340 the minimum value in $h(x, y)$ in Y20. This limitation is removed with the vertical
341 transformation 2 and the vertical stretching function introduced by Shchepetkin (2010), and
342 h_c can be any positive value. Here the Y21_VT experiment is conducted to examine the impact
343 of the vertical transformation in the ROMS model on seasonal Arctic sea ice simulation and
344 prediction, which uses the vertical transformation 2, the Shchepetkin stretching function, and
345 300 meters for h_c . As shown in Supplementary Figure S4-S5, compared to Y21_CTRL,
346 Y21_VT is less sensitive to the bathymetry and its layers are more evenly-distributed in the
347 upper 300 meters. With the changes of vertical layers of the upper ocean, the Y21_VT

350 experiment has minor SST changes relative to Y21_CTRL. The simulated temporal evolution
351 of total ice extent of Y21_VT (Fig. 4, red line) resembles to that of Y21_CTRL (Fig. 4, yellow
352 line), although some differences are seen at the regional scale in the areas with shallow water
353 (e.g., East Siberian, Laptev, Barents, and Kara Seas). The configuration of Y21_VT is used in
354 the following experiments.

355 It has been recognized that the tracer advection and the vertical mixing schemes have
356 important effects on ocean and sea ice simulation (e.g., Liang and Losch, 2018; Naughten et
357 al., 2017). Here the Y21_RP experiment is designated to explore the influence of different
358 advection schemes in the ROMS model. Specifically, the tracer advection scheme is changed
359 from the Multidimensional positive definite advection transport algorithm (MPDATA;
360 Smolarkiewicz, 2006) to the third-order upwind horizontal advection (U3H; Rasch, 1994;
361 Shchepetkin, and McWilliams, 2005) and the fourth-order centered vertical advection schemes
362 (C4V; Shchepetkin, and McWilliams, 1998; 2005). The MPDATA scheme applied in
363 Y20_MOD, Y21_CTRL, and Y21_VT is a non-oscillatory scheme but a sign preserving
364 scheme (Smolarkiewicz, 2006) that means MPDATA is not suitable for tracer fields having
365 both positive and negative values (i.e., temperature with degree Celsius in the ROMS model).
366 The upwind third-order (U3H) scheme used in Y21_RP is an oscillatory scheme but it
367 significantly reduces oscillations compared to other centered schemes (e.g., Hecht et al., 2000;
368 Naughten et al., 2017) available in the ROMS model.

369 Figure 8 shows the spatial distribution of the SST changes of Y21_VT and Y21_RP
370 relative to Y21_CTRL (as well as the OI SST and the difference between Y21_CTRL and

371 OISST). In general, Y21_CTRL shows cold prediction errors in the North Pacific (~2 degrees)
372 and the Atlantic (~3 degrees) compared to that of OISST in July, and these cold prediction
373 errors are enhanced as the prediction time increases (to 3-5 degrees, Fig. 8d-f). With the
374 U3H/C4V tracer advection scheme in Y21_RP, cold prediction errors shown in Y21_CTRL are
375 reduced significantly in the north Pacific and Atlantic, but SST under sea ice in much of the
376 Arctic Ocean is slightly colder than that of Y21_CTRL (Fig. 8j-l).

377 Y21_RP (Fig. 4, green line) shows comparable temporal evolution of the ice extent as
378 Y21_CTRL (as well as Y21_VT) until near the end of July. After that, the ice melting slows
379 down (closer to the observation) and the ice extent begins to recover earlier (after the first week
380 of September) in Y21_RP compared to Y21_CTRL. This leads to much smaller prediction error
381 in seasonal minimum ice extent relative to the observation. Y21_RP also shows better
382 predictive skill after late August compared with the CLIM/DAMP predictions (black dashed
383 and dotted lines). This suggests the delayed ice recovery in late September shown in Y20_MOD,
384 Y21_CTRL and Y21_VT is in part due to the choice of ocean advection and vertical mixing
385 schemes, which change the behavior of ocean state. At the regional scale, the slower ice decline
386 after July and earlier recovery of the ice extent in September mainly occur in the Beaufort-
387 Chukchi and Barents-Kara-Greenland Seas compared to that of Y21_CTRL (Fig. 4a, c). By
388 using U3H/C4V scheme, the Y21_RP experiment simulates higher sea ice concentration than
389 that of Y21_VT (Fig. 5f₁-f₃). For September, the Y21_RP experiment better predicts the ice
390 edge location in the Atlantic sector of the Arctic (i.e., smaller areas with horizontal/vertical
391 lining) compared to the experiments described above (not shown).

392 Figure 9 shows the evolution of sea ice mass budget terms of Y21_VT and Y21_RP.
393 Relative to Y21_VT, Y21_RP (with U3H/C4V scheme) results in increased frazil ice formation
394 in July, which is partly compensated by increased surface melting. Y21_RP also leads to
395 increased basal growth in mid- and late September (Fig. 9a, b).

396 Figure 10 shows the difference in the vertical profile of ocean temperature and salinity in
397 the upper 150 m averaged for the central Arctic Ocean between Y21_RP and Y21_VT. The
398 ocean temperature in the surface layer of Y21_RP is slightly colder during the prediction period
399 compared to that of Y21_VT (Fig. 10a), especially in August and September. Moreover, the
400 water in the surface layer (0-20 m) of Y21_RP is fresher than that of Y21_VT (Fig. 10b). They
401 reduce the freezing temperature and favor frazil ice formation. In the CAPS, the frazil ice
402 formation is determined by the freezing potential, which is the vertical integral of the difference
403 between temperature in upper ocean layer and the freezing temperature in the upper 5 m-layer.
404 The supercooled water is adjusted based on the freezing potential to form new ice and rejects
405 brine into the ocean that leads to saltier water between 20-50 m in Figure 10. It should be noted
406 that the increased frazil ice formation in July in Y21_RP might be also partly due to the
407 oscillatory behavior of U3H scheme, which makes the temperature fall below the freezing point
408 and then instantaneously forms new ice (as well as temperature/salinity adjustments).

409

410 **3.4. Impacts of sea ice thermodynamics in the CICE model**

411 In Y20, we used sea ice thermodynamics introduced by Bitz and Lipscomb (1999;
412 hereafter BL99) as the setup of CAPS, which assumes a fixed vertical salinity profile based on

413 observations. The new CICE model includes a MUSHY-layer ice thermodynamics introduced
414 by Turner et al. (2013), which simulates vertically and time-varying prognostic salinity and
415 associated effects on thermodynamic properties of sea ice. In the Y21_MUSHY experiment,
416 we change the ice thermodynamics from BL99 to MUSHY (Table 2) to examine whether
417 improved ice thermodynamics has noticeable influence on Arctic sea ice simulation and
418 prediction at seasonal timescale. Compared to Y21_RP, Y21_MUSHY (Fig. 4, pink line)
419 produces very similar evolution of the total ice extent. However, it simulates relatively larger
420 ice extent near the end of September, which is also reflected by the basin-wide increased ice
421 cover shown in Figure 5h₃. At the regional scale, compared to Y21_RP, Y21_MUSHY predicts
422 less ice in August in the Beaufort-Chukchi. The opposite is the case for the East Siberian-
423 Laptev Seas (Fig. 4a, b).

424 Figure 11 shows the difference of the ensemble mean of the predicted ice thickness
425 between Y21_MUSHY and Y21_RP. Compared with Y21_RP, Y21_MUSHY simulates
426 thicker ice (from ~0.2m in July to over 0.4m in September) extending from the Canadian Arctic,
427 through the central Arctic Ocean, to the Laptev Sea (Fig. 11a-c). This seems to be consistent
428 with previous studies, which show that the Mushy-layer thermodynamics simulates thicker ice
429 than BL99 thermodynamics in both standalone CICE (Turner and Hunke, 2015) and the fully-
430 coupled (Bailey et al., 2020), but Y21_MUSHY shows thinner ice (~0.2m) in an arc extending
431 from north of Alaska to north of eastern Siberia compared to Bailey et al. (2020). Note that
432 Y21_MUSHY focuses the effects of Mushy-thermodynamics on seasonal timescale while the
433 results in Bailey et al. (2020) are based on 50-year simulations.

434 Compared to Y21_RP, the mass budget of Y21_MUSHY (Fig. S6) shows that both surface
435 melting and frazil ice formation terms are increased. This compensation between surface
436 melting and frazil ice formation from the Mushy-layer thermodynamics in the CAPS leads to
437 relatively unchanged total ice extent between Y21_MUSHY and Y21_RP (Fig. 4 green and
438 pink lines).

439

440 **4. Prediction skill of CAPS at longer timescale**

441 The design of Arctic sea ice prediction experiments described above follow the protocol
442 of the Sea Ice Prediction Network (SPIN), in which the outlook start from June 1st, July 1st, and
443 August 1st to predict seasonal minimum of the ice extent in September. It is not clear that how
444 predictive skills of dynamical models participating in SIPN may change for longer period. Here
445 we conduct two more experiments to investigate the predictive capability of CAPS beyond the
446 SPIN prediction period. For the prediction experiments discussed above, we use a simple
447 approach to merge CryoSat-2 and SMOS ice thickness by replacing ice thickness less than 1m
448 in CryoSat-2 data with SMOS data for ice thickness assimilation. Ricker et al. (2017) presented
449 a new ice thickness product (CS2SMOS) based on the optimal interpolation to statistically
450 merge CrySat-2 and SMOS data. Here we utilize the configuration of Y21_RP but use
451 CS2SMOS SIT for the assimilation (Y21_SIT; Table 2). The predicted total ice extent is almost
452 identical to Y21_RP in July but slightly larger total extent after July than that of Y21_RP (not
453 shown). The configuration of Y21_SIT is used in the following experiments. Taking advantage
454 of the entire prediction period provided by CFS forecasts (7 months), the Y21_EXT-7

455 experiment is designed to extend the prediction period to the end of January next year (Table
456 2). Figure 12 shows the temporal evolution of the ensemble mean of the predicted total Arctic
457 sea ice extent (as well as regional ice extent) for Y21_EXT-7. The total ice extent exhibits
458 reasonable evolution in terms of seasonal minimum and timing of recovery compared with the
459 observations until late November. Y21_EXT-7 also performs better than that of the
460 CLIM/DAMP predictions (black dashed and dotted lines) until mid-to-late November. After
461 that, Y21_EXT-7 overestimates the total ice extent relative to the observations, and such
462 overestimation is largely contributed by more extensive sea ice in the Barents-Kara-Greenland
463 Seas (Fig. 12c), which is a result of a sharp increase in the basal growth term after mid-to-late
464 November (not shown).

465 A growing number of studies have shown evidences of Arctic sea ice spring predictability
466 barrier. It means that predictions initialized prior to spring (before May) have much lower
467 predictive skill than predictions initialized after/on that date (e.g., Bonan et al., 2019; Bushuk
468 et al., 2017; 2018; Day et al., 2014). To investigate the predictive capability of CAPS initialized
469 prior to the summer melting season, the Y21_MAR-7 experiment is initialized on March 1st,
470 2018 and predicts sea ice evolution until the end of September (Table 2). Figure 13 shows the
471 temporal evolution of the ensemble mean of the predicted total Arctic sea ice extent (as well as
472 regional ice extent) for the Y21_MAR-7 experiment. The evolution of predicted total sea ice
473 extent shows faster ice melting rate than the observations after mid-May, but slower ice
474 retreating after mid-July. As a result, the predicted minimum of ice extent has an overestimation
475 (~ 1.2 million km²) compared to the observed minimum. In contrast to Y21_MAR-7, the DAMP

476 prediction (black dotted line) agrees better with the observations throughout the 7-month
477 prediction period. At the regional scale, Y21_MAR-7 shows abrupt ice decline after May in the
478 Beaufort-Chukchi Seas (Fig. 13a), and this decline is mainly contributed by ice retreating along
479 the Alaskan coast (not shown). Sea ice in the East Siberian-Laptev Seas exhibits slow melting
480 after July (Fig. 13b), and ice cover still connect to the Siberian coast, which is different from
481 the observations (not shown). For the Barents-Kara-Greenland Seas (Baffin Bay-Canadian
482 Archipelago), there are systematic overestimations (underestimations) throughout the entire
483 prediction period (Fig. 13c-d). Bushuk et al. (2020) suggested that Arctic sea ice predictability
484 prior to the barrier date is mainly limited by synoptic events, which are only predictable for
485 few weeks, whereas the predictability after the barrier date is enhanced by ice-albedo feedback
486 with the onset of ice melting.

487

488 **5. Conclusions and Discussions**

489 This paper presents and evaluates the updated Coupled Arctic Prediction System (CAPS)
490 designated for Arctic sea ice prediction through a case study for the year of 2018. A set of Pan-
491 Arctic prediction experiments with improved/changed physical parameterizations as well as
492 different configurations starting from July 1st to the end of September are performed for 2018
493 to assess their impacts of the updated CAPS on the predictive skill of Arctic sea ice at seasonal
494 timescale. Specifically, we focus on the Rapid Refresh (RAP) physics in the WRF model, the
495 oceanic tracer advection scheme in the ROMS model, sea ice thermodynamics in the CICE
496 model, and investigate physical process linking them to Arctic sea ice simulation and prediction.

497 The results show that the updated CAPS with improved physical parameterizations can
498 better predict the evolution of the total ice extent compared with its predecessor described in
499 Yang et al. (2020), though the predictions exhibit some prediction errors in regional ice extent.
500 The key improvements of WRF, including cumulus, boundary layer, and land surface schemes,
501 result in improved simulations in downward radiative fluxes and near surface air temperature.
502 These improvements mainly influence the predicted ice thickness instead of total ice extent.
503 The difference in the predicted ice thickness can have potential impacts on the icebreakers
504 planning their routes across the ice-covered regions. The major changes of ROMS, including
505 tracer advection and vertical mixing schemes, reduces the prediction error in sea surface
506 temperature and changes ocean temperature and salinity structure in the surface layer, leading
507 to improved evolution of the predicted total ice extent (particularly correcting the late ice
508 recovery issue in the previous CAPS). The change of CICE, including improved ice
509 thermodynamics, have noticeable influences on the predicted ice thickness.

510 We demonstrate that CAPS can remain skillful beyond the designated period of Sea Ice
511 Prediction Network (SIPN), which has potential values for stakeholders making decisions
512 regarding the socioeconomical activities. Although CAPS shows extended predictive skill to
513 the freeze-up period, the prediction produces extensive ice through the basal growth near the
514 end of prediction. The excessive basal growth may be partly due to that the bias of the CFS
515 data propagates into the model domain through lateral boundary conditions and its accumulated
516 effect influences Arctic sea ice simulation during the freeze-up period.

517 Keen et al. (2021) analyzed the Arctic mass budget of 15 models participated in the

518 Coupled Model Intercomparison Project Phase 6 (CMIP6). We notice that, first, the top melting
519 and the basal melting terms in CMIP6 models have comparable contributions in July while the
520 top melting term only has ~50% contribution relative to the basal melting term in the CAPS.
521 The updated CAPS with the RAP physics improves the performance of shortwave/longwave
522 radiation at the surface (Fig. 1 and Fig. 2). The net flux at the surface, however, may still be
523 underestimated in the CAPS. Besides, the surface property of sea ice (i.e., the amount of melt
524 ponds, bare ice, and snow) is a factor that influences surface albedo and thus the absorbed
525 shortwave radiation (e.g., Nicolaus et al., 2012; Nicolaus and Katlein, 2013). The prediction
526 experiments starting at July 1st in this study do not consider the initialization of melt ponds (i.e.,
527 zero melt pond coverage at the initial). However, melt ponds start to develop in early May
528 based on the satellite observations (e.g., Liu et al., 2015, Fig. 1). The initialization of melt pond
529 based on the observations (e.g., Ding et al., 2020) in the CAPS is a direction to improve the
530 representation of the ice surface properties. Second, the mass budget analysis by both Keen et
531 al. (2021) and this study show that the contribution of lateral melting term is relatively small,
532 which might be due to that CMIP6 models and the CAPS assume constant floe-size (i.e., 300
533 meters in CICE), which is a critical value to determine the strength of lateral melting (e.g.,
534 Horvat et al., 2016; Steele, 1992). Recently, several studies have proposed floe size distribution
535 models (e.g., Bateson et al., 2020; Bennetts et al., 2017; Boutin et al., 2020; Horvat and
536 Tziperman, 2015; Roach et al., 2018, 2019; Zhang et al., 2015, 2016). Incorporating floe size
537 distribution model in the CAPS and understanding its impacts on seasonal Arctic sea ice
538 prediction will be a future direction of developing CAPS. Lastly, the prediction experiments

539 with the upwind advection scheme (i.e., Y21_RP, Y21_EXT-7) shows spurious large frazil ice
540 formation, particularly in July, which is different from the analysis shown in Keen et al. (2021).
541 An approach for reducing spurious frazil ice formation is proposed by Naughten et al. (2017)
542 that they implemented upwind limiter (Leonard and Mokhtari, 1990) to the U3H scheme to
543 further reduce the oscillations. Naughten et al. (2018) also suggested that the oscillatory
544 behaviors can be smoothed out by applying the Akima fourth-order tracer advection scheme
545 combined with Laplacian horizontal diffusion at a level strong enough. Beside of the oscillatory
546 behaviors of advection scheme, the ice-ocean heat flux can also play a role in the spurious frazil
547 ice formation. As discussed in section 3.3, the freezing/melting potential not only determines
548 the amount of newly-formed ice, but also limits the amount of energy that can be extracted
549 from the ocean surface layer to melt sea ice. This implies that the ocean surface layer will be
550 close to the freezing temperature if the ice-ocean heat fluxes reach the limit imposed by the
551 melting potential. Shi et al. (2021) discussed the impacts of different ice-ocean heat flux
552 parametrizations on sea ice simulations. Their results suggest that Arctic sea ice will be thicker
553 and ocean temperature will warmer beneath high-concentration ice with a complex approach
554 proposed by Schmidt et al. (2004) that limits melt rates (heat fluxes) of sea ice through
555 considering a fresh water layer underlying sea ice. The warmer ocean temperature under sea
556 ice with a more complex approach in ice-ocean heat flux may be the solution to reduce the
557 occurrence of local temperature falling below freezing temperature with oscillatory advection
558 schemes.

559 Based on the prediction experiments discussed in this paper, the configuration with the

560 RAP physics, the U3H/C4V ocean advection, BL99 ice thermodynamics, and CS2SMOS ice
561 thickness assimilation (Table 2, Y21_SIT) is assigned as the finalized CAPS version 1.0.
562 Improving the representation of physical processes in the CAPS version 1.0 for further
563 reducing the model bias will remain the main focus for the development of CAPS. Since the
564 CAPS is a regional modeling system, it relies on the forecasts from global climate models as
565 initial and lateral boundary conditions. That is, biases existed in GCM simulations (here the
566 CFS forecast) can be propagated into and affect the entire area-limited domain (e.g., Bruyère
567 et al., 2014; Rocheta et al., 2020; Wu et al., 2005). This issue can be a potential source that
568 influences the predictive capability of CAPS for longer timescales. Studies have applied bias
569 correction techniques with different complexities for improving the performance of regional
570 modeling system (e.g., Bruyère et al., 2014; Colette et al., 2012; Rocheta et al., 2017, 2020).
571 Further investigation is needed to address biases inherited from GCM predictions through
572 lateral boundaries for improving the predictive capability of CAPS.
573

574 Code and data availability: The COAWST and CICE models are open source and can be
575 downloaded from their developers at <https://github.com/jcwarner-usgs/COAWST> and
576 <https://github.com/CICE-Consortium/CICE>, respectively. PDAF can be obtained from
577 <https://pdaf.awi.de/trac/wiki>. CAPS v1.0 described in this paper is permanently archived at
578 <https://doi.org/10.5281/zenodo.5034971>. The prediction data analyzed in this paper can be
579 accessed from <https://doi.org/10.5281/zenodo.4911415>.

580

581 Author contributions: CYY and JL designed the model experiments, developed the
582 updated CAPS model, and wrote the manuscript, CYY conducted the prediction experiments
583 and analyzed the results. DC provided constructive feedback on the manuscript.

584

585 Competing interests: The authors declare that they have no conflict of interest.

586

587 Acknowledgements: This research is supported by the National Natural Science
588 Foundation of China (42006188), the National Key R&D Program of China
589 (2018YFA0605901), and the Innovation Group Project of Southern Marine Science and
590 Engineering Guangdong Laboratory (Zhuhai) (311021008). The authors also acknowledge the
591 National Centers for Environmental Prediction for providing CFS seasonal forecasts, the
592 University of Hamburg for distributing the SMOS sea ice thickness data, the Alfred-Wegener-
593 Institut, Helmholtz Zentrum für Polar- und Meeresforschung for providing the CryoSat-2 sea
594 ice thickness data and CS2SMOS data, the Polar Science Center for distributing the PIOMAS
595 ice thickness data, the National Snow and Ice Data Center for providing the SSMIS sea ice
596 concentration data, the European Centre for Medium-Range Weather Forecasts for distributing
597 the ERA5 reanalysis, and the National Oceanic and Atmospheric Administration for providing
598 the OI sea surface temperature.

599 **6. References**

- 600 Aagaard, K.: A synthesis of the Arctic Ocean circulation. *Rapp. P.-V. Reun.- Cons. Int. Explor.*
601 *Mer*, 188, 11–22, 1989.
- 602 Bailey, D. A., Holland, M. M., DuVivier, A. K., Hunke, E. C., and Turner, A. K.: Impact of a
603 new sea ice thermodynamic formulation in the CESM2 sea ice component. *Journal of*
604 *Advances in Modeling Earth Systems*, 12, e2020MS002154.
605 <https://doi.org/10.1029/2020MS002154>, 2020.
- 606 Bateson, A. W., Feltham, D. L., Schröder, D., Hosekova, L., Ridley, J. K., and Aksenov, Y.:
607 Impact of sea ice floe size distribution on seasonal fragmentation and melt of Arctic sea
608 ice, *The Cryosphere*, 14, 403–428, <https://doi.org/10.5194/tc-14-403-2020>, 2020.
- 609 Bitz, C. M. and Lipscomb, W. H.: An energy-conserving thermodynamic sea ice model for
610 climate study. *J. Geophys. Res.-Oceans*, 104, 15669–15677, 1999.
- 611 Benjamin, S. G., Weygandt, S. S., Brown, J. M., Hu, M., Alexander, C. R., Smirnova, T. G.
612 and Manikin, G. S.: A North American hourly assimilation and model forecast cycle: the
613 Rapid Refresh. *Monthly Weather Review*, 144, 1669–1694.
614 <https://doi.org/10.1175/MWR-D-15-0242.1>, 2016.
- 615 Bennetts, L. G., O'Farrell, S., and Uotila, P.: Brief communication: Impacts of ocean-wave-
616 induced breakup of Antarctic sea ice via thermodynamics in a stand-alone version of the
617 CICE sea-ice model, *The Cryosphere*, 11, 1035–1040, [https://doi.org/10.5194/tc-11-](https://doi.org/10.5194/tc-11-1035-2017)
618 [1035-2017](https://doi.org/10.5194/tc-11-1035-2017), 2017.
- 619 Biswas, M. K., Zhang, J. A., Grell, E., Kalina, E., Newman, K., Bernardet, L., Carson, L.,
620 Frimel, J., and Grell, G.: Evaluation of the Grell–Freitas Convective Scheme in the
621 Hurricane Weather Research and Forecasting (HWRF) Model, *Weather and Forecasting*,
622 35(3), 1017–1033, 2020.
- 623 Blanchard-Wrigglesworth, E., Bitz, C., and Holland, M.: Influence of initial conditions and
624 climate forcing on predicting Arctic sea ice. *Geophysical Research Letters*, 38, L18503.
625 <https://doi.org/10.1029/2011GL048807>, 2011.

626 Blanchard-Wrigglesworth, E., and Bushuk, M.: Robustness of Arctic sea-ice predictability in
627 GCMs. *Climate Dynamics*, 52, 5555–5566, 2018.

628 Blanchard-Wrigglesworth, E., Cullather, R., Wang, W., Zhang, J., and Bitz, C. M.: Model
629 forecast skill and sensitivity to initial conditions in the seasonal sea ice outlook.
630 *Geophysical Research Letters*, 42, 8042–8048. <https://doi.org/10.1002/2015GL065860>,
631 2015.

632 Bonan, D., Bushuk, M., and Winton, M.: A spring barrier for regional predictions of summer
633 Arctic sea ice. *Geophysical Research Letter*, 46, 5937–5947.
634 <https://doi.org/10.1029/2019GL082947>, 2019.

635 Boutin, G., Lique, C., Ardhuin, F., Rousset, C., Talandier, C., Accensi, M., and Girard-Ardhuin,
636 F.: Towards a coupled model to investigate wave–sea ice interactions in the Arctic
637 marginal ice zone, *The Cryosphere*, 14, 709–735, [https://doi.org/10.5194/tc-14-709-](https://doi.org/10.5194/tc-14-709-2020)
638 2020, 2020.

639 Briegleb, B. P. and Light, B.: A Delta-Eddington multiple scattering parameterization for solar
640 radiation in the sea ice component of the Community Climate System Model. NCAR
641 Tech. Note NCAR/TN-472+STR, National Center for Atmospheric Research, 2007.

642 Bruyère, C. L., Done, J. M., Holland, G. J., and Fredrick, S.: Bias corrections of global models
643 for regional climate simulations of high-impact weather. *Clim Dyn* 43, 1847–1856
644 (2014). <https://doi.org/10.1007/s00382-013-2011-6>, 2014.

645 Bushuk, M., Msadek, R., Winton, M., Vecchi, G., Gudgel, R., Rosati, A., and Yang, X.: Skillful
646 regional prediction of Arctic sea ice on seasonal timescales. *Geophysical Research Letter*,
647 44, 4953–4964. <https://doi.org/10.1002/2017GL073155>, 2017.

648 Bushuk, M., Msadek, R., Winton, M., Vecchi, G., Yang, X., Rosati, A., and Gudgel, R.:
649 Regional Arctic sea-ice prediction: Potential versus operational seasonal forecast skill.
650 *Climate Dynamics*, 52, 2721–2743, 2018.

651 Bushuk, M., Winton, M., Bonan, D. B., Blanchard-Wrigglesworth, E., and Delworth, T. L.: A
652 mechanism for the Arctic sea ice spring predictability barrier. *Geophysical Research*
653 *Letters*, 47, e2020GL088335. <https://doi.org/10.1029/2020GL088335>, 2020.

654 Carmack, E., Polyakov, I., Padman, L., Fer, I., Hunke, E., Hutchings, J., Jackson, J., Kelley,
655 D., Kwok, R., Layton, C., Melling, H., Perovich, D., Persson, O., Ruddick, B.,
656 Timmermans, M.-L., Toole, J., Ross, T., Vavrus, S., and Winsor, P.: Toward Quantifying
657 the Increasing Role of Oceanic Heat in Sea Ice Loss in the New Arctic. *Bulletin of the*
658 *American Meteorological Society* 96, 12, 2079-2105, [https://doi.org/10.1175/BAMS-D-](https://doi.org/10.1175/BAMS-D-13-00177.1)
659 [13-00177.1](https://doi.org/10.1175/BAMS-D-13-00177.1), 2015.

660 Cavalieri, D. J., Parkinson, C. L., Gloersen, P., and Zwally, H. J.: updated yearly. *Sea Ice*
661 *Concentrations from Nimbus-7 SMMR and DMSP SSM/I-SSMIS Passive Microwave*
662 *Data, Version 1. Boulder, Colorado USA. NASA National Snow and Ice Data Center*
663 *Distributed Active Archive Center.* <https://doi.org/10.5067/8GQ8LZQVLOVL>, 1996.

664 Chen, F. and Dudhia, J.: Coupling an advanced land surface–hydrology model with the Penn
665 State–NCAR MM5 modeling system. Part I: Model implementation and sensitivity. *Mon.*
666 *Wea. Rev.*, 129, 569–585, 2001.

667 Chevallier, M., Salas y Mélia, D., Voldoire, A., Déqué, M., and Garric, G.: Seasonal forecasts
668 of the pan-Arctic sea ice extent using a GCM-based seasonal prediction system. *Journal*
669 *of Climate*, 26(16), 6092–6104, 2013.

670 Colette, A., Vautard, R., and Vrac, M.: Regional climate downscaling with prior statistical
671 correction of the global climate forcing, *Geophys. Res. Lett.*, 39, L13707,
672 <https://doi.org/10.1029/2012GL052258>, 2012.

673 Day, J. J., Tietsche, S., Collins, M., Goessling, H. F., Guemas, V., Guillory, A., et al.: The
674 Arctic predictability and prediction on seasonal-to-interannual timescales (apposite) data
675 set version 1. *Geoscientific Model Development*, 9, 2255–2270, 2016.

676 Day, J., Tietsche, S., and Hawkins, E.: Pan-Arctic and regional sea ice predictability:
677 Initialization month dependence. *Journal of Climate*, 27(12), 4371–4390, 2014.

678 Ding, Y., Cheng, X., Liu, J., Hui, F., Wang, Z., and Chen, S.: Retrieval of Melt Pond Fraction
679 over Arctic Sea Ice during 2000–2019 Using an Ensemble-Based Deep Neural Network.
680 Remote Sensing. 12(17):2746. <https://doi.org/10.3390/rs12172746>, 2020

681 DuVivier, A. K., Holland, M. M., Landrum, L., Singh, H. A., Bailey, D. A., and Maroon, E.
682 A.: Impacts of sea ice mushy thermodynamics in the Antarctic on the coupled Earth
683 system. Geophysical Research Letters, 48, e2021GL094287.
684 <https://doi.org/10.1029/2021GL094287>, 2021.

685 Fer, I.: Near-inertial mixing in the central Arctic Ocean. J. Phys. Oceanogr., 44, 2031–2049,
686 <https://doi.org/10.1175/JPO-D-13-0133.1>, 2014.

687 Fetterer, F., Knowles, K., Meier, W. N., Savoie, M., and Windnagel, A. K.: updated daily. Sea
688 Ice Index, Version 3. Boulder, Colorado USA. NSIDC: National Snow and Ice Data
689 Center. <https://doi.org/10.7265/N5K072F8>, 2017.

690 Freitas, S. R., Grell, G. A., Molod, A., Thompson, M. A., Putman, W. M., Santos e Silva, C.
691 M. and Souza, E. P.: Assessing the Grell–Freitas convection parameterization in the
692 NASA GEOS modeling system. J. Adv. Model. Earth Syst., 10, 1266–1289,
693 <https://doi.org/10.1029/2017MS001251>, 2018.

694 Freitas, S. R., Grell, G. A., and Li, H.: The Grell–Freitas (GF) convection parameterization:
695 recent developments, extensions, and applications, Geosci. Model Dev., 14, 5393–5411,
696 <https://doi.org/10.5194/gmd-14-5393-2021>, 2021.

697 Germe, A., Chevallier, M., y Mélia, D. S., Sanchez-Gomez, E., and Cassou, C.: Interannual
698 predictability of Arctic sea ice in a global climate model: Regional contrasts and
699 temporal evolution. Climate Dynamics, 43(9-10), 2519–2538, 2014.

700 Grell, G. A., and Freitas, S.: A scale and aerosol aware stochastic convective parameterization
701 for weather and air quality modeling. Atmos. Chem. Phys., 14, 5233–5250,
702 <https://doi.org/10.5194/acp-14-5233-2014>, 2014.

703 Guemas, V., Blanchard-Wrigglesworth, E., Chevallier, M., Day, J. J., Déqué, M., Doblus-
704 Reyes, F. J., et al.: A review on Arctic sea-ice predictability and prediction on seasonal

705 to decadal time-scales. *Quarterly Journal of the Royal Meteorological Society*, 142(695),
706 546–561, 2016.

707 Haidvogel, D. B., Arango, H., Budgell, W. P., Cornuelle, B. D., Curchitser, E., Di Lorenzo, E.,
708 et al.: Ocean forecasting in terrain-following coordinates: Formulation and skill
709 assessment of the Regional Ocean Modeling System, *Journal of Computational Physics*,
710 227, 3595–3624, 2008.

711 Hecht, M. W., Wingate, B. A., and Kassis, P.: A better, more discriminating test problem for
712 ocean tracer transport. *Ocean Modell.* 2 (1–2), 1–15. [https://doi.org/10.1016/S1463-50](https://doi.org/10.1016/S1463-5003(00)00004-4)
713 [03\(00\)00004-4](https://doi.org/10.1016/S1463-5003(00)00004-4), 2000.

714 Hersbach, H., Bell, B., Berrisford, P., et al.: The ERA5 global reanalysis. *Quarterly Journal of*
715 *the Royal Meteorological Society*, 146, 1999–2049. <https://doi.org/10.1002/qj.3803>,
716 2020.

717 Horvat, C., and Tziperman, E.: A prognostic model of the sea-ice floe size and thickness
718 distribution. *Cryosphere* 9, 2119–2134, 2015.

719 Horvat, C., Tziperman, E., and Campin, J.-M.: Interaction of sea ice floe size, ocean eddies,
720 and sea ice melting. *Geophysical Research Letters*, 43, 8083–8090.
721 <https://doi.org/10.1002/2016GL069742>, 2016.

722 Huang, Y., Chou, G., Xie, Y., & Soulard, N.: Radiative control of the interannual variability
723 of Arctic sea ice. *Geophysical Research Letters*, 46, 9899– 9908.
724 <https://doi.org/10.1029/2019GL084204>, 2019.

725 Itoh, M., Nishino, S., Kawaguchi, Y., and Kikuchi, T.: Barrow Canyon volume, heat, and
726 freshwater fluxes revealed by long-term mooring observations between 2000 and 2008.
727 *J. Geophys. Res. Oceans*, 118, 4363–4379, <https://doi.org/10.1002/jgrc.20290>, 2013.

728 Jung, T., Gordon, N.D., Bauer, P., Bromwich, D.H., Chevallier, M., Day, J.J., Dawson, J.,
729 Doblas-Reyes, F., Fairall, C., Goessling, H.F., Holland, M., Inoue, J., Iversen, T., Klebe,
730 S., Lemke, P., Losch, M., Makshtas, A., Mills, B., Nurmi, P., Perovich, D., Reid, P.,
731 Renfrew, I.A., Smith, G., Svensson, G., Tolstykh, M., and Yang, Q.: Advancing Polar

732 Prediction Capabilities on Daily to Seasonal Time Scales. *Bulletin of the American*
733 *Meteorological Society*. <https://doi.org/10.1175/BAMS-D-14-00246.1>, 2016.

734 Kaleschke, L., Tian-Kunze, X., Maaß, N., Mäkynen, M., and Drusch, M.: Sea ice thickness
735 retrieval from SMOS brightness temperatures during the Arctic freeze-up period.
736 *Geophys. Res. Lett.*, L05501, <https://doi.org/10.1029/2012GL050916>, 2012.

737 Kapsch, M., Graversen, R. G., Tjernström, M., and Bintanja, R.: The Effect of Downwelling
738 Longwave and Shortwave Radiation on Arctic Summer Sea Ice. *Journal of Climate* 29,
739 3, 1143-1159, <https://doi.org/10.1175/JCLI-D-15-0238.1>, 2016.

740 Kay, J. E., L'Ecuyer, T., Gettelman, A., Stephens, G., and O'Dell, C.: The contribution of cloud
741 and radiation anomalies to the 2007 Arctic sea ice extent minimum, *Geophys. Res. Lett.*,
742 35, L08503, doi:10.1029/2008GL033451, 2008.

743 Keen, A., Blockley, E., Bailey, D. A., Boldingh Debernard, J., Bushuk, M., Delhaye, S.,
744 Docquier, D., Feltham, D., Massonnet, F., O'Farrell, S., Ponsoni, L., Rodriguez, J. M.,
745 Schroeder, D., Swart, N., Toyoda, T., Tsujino, H., Vancoppenolle, M., and Wyser, K.:
746 An inter-comparison of the mass budget of the Arctic sea ice in CMIP6 models, *The*
747 *Cryosphere*, 15, 951–982, <https://doi.org/10.5194/tc-15-951-2021>, 2021.

748 Kirkman, C. H., IV, and Bitz, C. M.: The Effect of the Sea Ice Freshwater Flux on Southern
749 Ocean Temperatures in CCSM3: Deep-Ocean Warming and Delayed Surface Warming.
750 *Journal of Climate* 24, 9, 2224-2237, <https://doi.org/10.1175/2010JCLI3625.1>, 2011.

751 Kwok, R.: Arctic sea ice thickness, volume, and multiyear ice coverage: Losses and coupled
752 variability (1958–2018). *Environmental Research Letters*, 13(10), 105005, 2018

753 Laxon, S., Giles, K. A., Ridout, A. L., Wingham, D. J., Willatt, R., Cullen, R., Kwok, R.,
754 Schweiger, A., Zhang, J., Haas, C., Hendricks, S., Krishfield, R., Kurtz, N., Farrell, S.,
755 and Davidson, M.: CryoSat-2 estimates of Arctic sea ice thickness and volume, *Geophys.*
756 *Res. Lett.*, 40, <https://doi.org/10.1002/grl.50193>, 2013.

757 Lemieux, J. F., Dupont, F., Blain, P., Roy, F., Smith, G. C., and Flato, G. M.: Improving the
758 simulation of landfast ice by combining tensile strength and a parameterization for

759 grounded ridges. *J. Geophys. Res. Oceans*, 121:7354–7368,
760 <http://dx.doi.org/10.1002/2016JC012006>, 2016.

761 Leonard, B., Mokhtari, S.: ULTRA-SHARP Non oscillatory Convection Schemes for High-
762 Speed Steady Multidimensional Flow. Technical Report. NASA, 1990.

763 Liang, X., and Losch, M.: On the effects of increased vertical mixing on the Arctic Ocean and
764 sea ice. *Journal of Geophysical Research: Oceans*, 123, 9266– 9282.
765 <https://doi.org/10.1029/2018JC014303>, 2018.

766 Liu, J., Song, M., Horton, R., and Hu, Y.: Revisiting the potential of melt pond fraction as a
767 predictor for the seasonal Arctic sea ice minimum. *Environmental Research Letters*, 10,
768 054017. <https://doi.org/10.1088/1748-9326/10/5/054017>, 2015.

769 Liu, J., Chen, Z., Hu, Y., Zhang, Y., Ding, Y., Cheng, X., et al.: Towards reliable arctic sea ice
770 prediction using multivariate data assimilation. *Science Bulletin*, 64(1), 63–72, 2019.

771 Merryfield, W., Lee, W.-S., Wang, W., Chen, M., and Kumar, A.: Multi-system seasonal
772 predictions of Arctic sea ice. *Geophysical Research Letters*, 40, 1551–1556.
773 <https://doi.org/10.1002/grl.50317>, 2013.

774 Mallett, R. D. C., Stroeve, J. C., Cornish, S. B. Crawford, A. D., Lukovich, J. V., Serreze, M.
775 C., Barrett, A. P., Meier, W. N., Heorton, H. D. B. S., and Tsamados, M.: Record winter
776 winds in 2020/21 drove exceptional Arctic sea ice transport. *Commun Earth Environ* 2,
777 149, <https://doi.org/10.1038/s43247-021-00221-8>, 2021.

778 Maslanik, J. and Stroeve, J.: Near-Real-Time DMSP SSMIS Daily Polar Gridded Sea Ice
779 Concentrations, Version 1. Boulder, Colorado USA. NASA National Snow and Ice Data
780 Center Distributed Active Archive Center. <https://doi.org/10.5067/U8C09DWVX9LM>,
781 1999.

782 McLaughlin, F. A., Carmack, E. C., Williams, W. J., Zimmerman, S., Shimada, K., and Itoh,
783 M.: Joint effects of boundary currents and thermohaline intrusions on the warming of
784 Atlantic water in the Canada Basin, 1993–2007. *J. Geophys. Res.*, 114, C00A12,
785 <https://doi.org/10.1029/2008JC005001>, 2009.

786 Meehl, G.A., Stocker, T. F., Collins, W. D., et al.: Global Climate Projections. In: Climate
787 Change 2007: The Physical Science Basis. Contribution of Working Group I to the
788 Fourth Assessment Report of the Intergovernmental Panel on Climate Change [Solomon,
789 S., D. Qin, M. Manning, Z. Chen, M. Marquis, K.B. Averyt, M. Tignor and H.L. Miller
790 (eds.)]. Cambridge University Press, Cambridge, United Kingdom and New York, NY,
791 USA, 2007.

792 Msadek, R., Vecchi, G., Winton, M., and Gudgel, R.: Importance of initial conditions in
793 seasonal predictions of Arctic sea ice extent. *Geophysical Research Letters*, 41, 5208–
794 5215. <https://doi.org/10.1002/2014GL060799>, 2014.

795 Nakanishi, M., and Niino., H.: Development of an improved turbulence closure model for the
796 atmospheric boundary layer. *J. Meteor. Soc. Japan*, 87, 895–912,
797 <https://doi.org/10.2151/jmsj.87.895>, 2009.

798 Naughten, K. A., Galton-Fenzi, B. K., Meissner, K. J., England, M. H., Brassington, G. B.,
799 Colberg, F., Hattermann, T., and Debernard, J. B.: Spurious sea ice formation caused by
800 oscillatory ocean tracer advection schemes. *Ocean Model.*, 116, 108–117, 2017.

801 Naughten, K. A., Meissner, K. J., Galton-Fenzi, B. K., England, M. H., Timmermann, R.,
802 Hellmer, H. H., Hattermann, T., and Debernard, J. B.: Intercomparison of Antarctic ice-
803 shelf, ocean, and sea-ice interactions simulated by MetROMS-iceshelf and FESOM 1.4.
804 *Geosci. Model. Dev.*, 11, 1257–1292, 2018

805 Nerger, L., and Hiller, W.: Software for Ensemble-based Data Assimilation Systems -
806 Implementation Strategies and Scalability. *Computers and Geosciences*, 55, 110-118.
807 <https://doi.org/10.1016/j.cageo.2012.03.026>, 2013.

808 Nerger, L., Janjić, T., Schröter, J. and Hiller, W.: A unification of ensemble square root Kalman
809 filters. *Monthly Weather Review*, 140, 2335-2345. [https://doi.org/10.1175/MWR-D-11-](https://doi.org/10.1175/MWR-D-11-00102.1)
810 [00102.1](https://doi.org/10.1175/MWR-D-11-00102.1), 2012.

811 Newton, R., Pfirman, S., Schlosser, P., Tremblay, B., Murray, M. and Pomerance, R.: White
812 Arctic vs. Blue Arctic: A case study of diverging stakeholder responses to environmental
813 change. *Earth's Future*, 4: 396-405. <https://doi.org/10.1002/2016EF000356>, 2016.

814 Nicolaus M., Katlein, C., Maslanik, J., and Hendricks, S.: Changes in Arctic sea ice result in
815 increasing light transmittance and absorption. *Geophysical Research Letters*, 39, L24501.
816 <https://doi.org/10.1029/2012GL053738>, 2012

817 Nicolaus M., and Katlein, C.: Mapping radiation transfer through sea ice using a remotely
818 operated vehicle (ROV). *The Cryosphere*, 7, 763-77. [https://doi.org/10.5194/tc-7-763-](https://doi.org/10.5194/tc-7-763-2013)
819 2013, 2013.

820 Notz, D., Jahn, A., Holland, M., Hunke, E., Massonnet, F., Stroeve, J., Tremblay, B., and
821 Vancoppenolle, M.: The CMIP6 Sea-Ice Model Intercomparison Project (SIMIP):
822 understanding sea ice through climate-model simulations, *Geosci. Model Dev.*, 9, 3427–
823 3446, <https://doi.org/10.5194/gmd-9-3427-2016>, 2016.

824 Ogi, M., Yamazaki, K., and Wallace, J. M.: Influence of winter and summer surface wind
825 anomalies on summer Arctic sea ice extent, *Geophys. Res. Lett.*, 37, L07701,
826 [doi:10.1029/2009GL042356](https://doi.org/10.1029/2009GL042356), 2010.

827 Olonscheck, D., Mauritsen, T. and Notz, D.: Arctic sea-ice variability is primarily driven by
828 atmospheric temperature fluctuations. *Nat. Geosci.* 12, 430–434,
829 <https://doi.org/10.1038/s41561-019-0363-1>, 2019.

830 Padman, L., and Dillon, T. M.: Vertical heat fluxes through the Beaufort Sea thermohaline
831 staircase. *J. Geophys. Res.*, 92, 10 799–10 806,
832 <https://doi.org/10.1029/JC092iC10p10799>, 1987.

833 Perovich, D., Richter-Menge, J., Jones, K., Light, B., Elder, B., Polashenski, C., Laroche, D.,
834 Markus, T., and Lindsay, R.: Arctic sea-ice melt in 2008 and the role of solar heating.
835 *Annals of Glaciology*, 52(57), 355-359. [doi:10.3189/172756411795931714](https://doi.org/10.3189/172756411795931714), 2011.

836 Perovich, D., Richter-Menge, J., Polashenski, C., Elder, B., Arbetter, T., and Brennick, O.: Sea
837 ice mass balance observations from the North Pole Environmental Observatory,
838 *Geophys. Res. Lett.*, 41, 2019– 2025, doi:10.1002/2014GL059356, 2014.

839 Peterson, K., Arribas, A., Hewitt, H., Keen, A., Lea, D., and McLaren, A.: Assessing the
840 forecast skill of Arctic sea ice extent in the GloSea4 seasonal prediction system. *Climate*
841 *Dynamics*, 44(1-2), 147–162, 2015.

842 Pham, D. T.: Stochastic methods for sequential data assimilation in strongly nonlinear systems.
843 *Mon. Wea. Rev.*, 129, 1194–1207, 2001.

844 Rasch, P. J.: Conservative shape-preserving two-dimensional transport on a spherical reduced
845 grid, *Mon. Wea. Rev.*, 122, 1337-1350, 1994.

846 Reynolds, R. W., Smith, T. M., Liu, C., Chelton, D. B., Casey, K. S., and Schlax, M. G.: Daily
847 High-Resolution-Blended Analyses for Sea Surface Temperature, *Journal of Climate*,
848 20(22), 5473-5496, 2007.

849 Ricker, R., Hendricks, S., Kaleschke, L., Tian-Kunze, X., King, J., and Haas, C.: A weekly
850 Arctic sea-ice thickness data record from merged CryoSat-2 and SMOS satellite data,
851 *The Cryosphere*, 11, 1607–1623, <https://doi.org/10.5194/tc-11-1607-2017>, 2017.

852 Roach, L. A., Bitz, C. M., Horvat, C., and Dean, S. M.: Advances in modeling interactions
853 between sea ice and ocean surface waves. *Journal of Advances in Modeling Earth*
854 *Systems*, 11. <https://doi.org/10.1029/2019MS001836>, 2019.

855 Roach, L. A., Horvat, C., Dean, S. M., and Bitz, C. M.: An emergent sea ice floe size
856 distribution in a global coupled ocean–sea ice model. *Journal of Geophysical Research:*
857 *Oceans*, 123(6), 4322–4337. <https://doi.org/10.1029/2017JC013692>, 2018.

858 Rocheta, E., Evans, J. P., and Sharma, A.: Can Bias Correction of Regional Climate Model
859 Lateral Boundary Conditions Improve Low-Frequency Rainfall Variability?, *Journal of*
860 *Climate*, 30(24), 9785-9806, 2017.

861 Rocheta, E., Evans, J. P. and Sharma, A.: Correcting lateral boundary biases in regional climate
862 modelling: the effect of the relaxation zone. *Clim. Dyn.*, 55, 2511–2521.
863 <https://doi.org/10.1007/s00382-020-05393-1>, 2020.

864 Serreze, M. C. and Meier, W. N.: The Arctic's sea ice cover: trends, variability, predictability,
865 and comparisons to the Antarctic. *Ann. N.Y. Acad. Sci.*, 1436: 36-53.
866 <https://doi.org/10.1111/nyas.13856>, 2019.

867 Saha, S., Moorthi, S., Wu, X., et al.: The NCEP climate forecast system version 2. *J. Clim.*
868 27:2185–2208, 2014.

869 Schmidt, G. A., Bitz, C. M., Mikolajewicz, U., and Tremblay, L.-B.: Ice–ocean boundary
870 conditions for coupled models, *Ocean Model.*, 7, 59–74, 2004.

871 Shchepetkin, A.F., McWilliams, J. C.: Quasi-monotone advection schemes based on explicit
872 locally adaptive dissipation. *Mon. Weather Rev.* 126 (6), 1541–1580, 1998.

873 Shchepetkin, A. F., and McWilliams, J. C.: The Regional Ocean Modeling System: A split-
874 explicit, free-surface, topography following coordinates ocean model, *Ocean Modelling*,
875 9, 347-404, 2005.

876 Shi, X., Notz, D., Liu, J., Yang, H., and Lohmann, G.: Sensitivity of Northern Hemisphere
877 climate to ice–ocean interface heat flux parameterizations, *Geosci. Model Dev.*, 14,
878 4891–4908, <https://doi.org/10.5194/gmd-14-4891-2021>, 2021.

879 Sigmond, M., Fyfe, J., Flato, G., Kharin, V., and Merryfield, W.: Seasonal forecast skill of
880 Arctic sea ice area in a dynamical forecast system. *Geophysical Research Letters*, 40,
881 529–534. <https://doi.org/10.1002/grl.50129>, 2013.

882 Skamarock, W. C., Klemp, J. B., Dudhia, J., Gill, D. O., Barker, D. M., Wang, W. and Powers,
883 J. G.: A Description of the Advanced Research WRF Version 2. NCAR Technical Note,
884 NCAR/TN-468+STR, 2005.

885 Smolarkiewicz, P. K.: Multidimensional positive definite advection transport algorithm: An
886 overview. *Int. J. Numer. Methods Fluids*, 50, 1123–1144, 2006.

887 Song, Y. and Haidvogel, D. B.: A semi-implicit ocean circulation model using a generalized
888 topography-following coordinate system. *J. Comp. Phys.*, 115(1), 228-244, 1994.

889 Steele, M.: Sea ice melting and floe geometry in a simple ice-ocean model. *Journal of*
890 *Geophysical Research: Oceans*, 97(C11), 17,729–17,738.
891 <https://doi.org/10.1029/92JC01755>, 1992.

892 Stroeve, J., Blanchard-Wrigglesworth, E., Guemas, V., Howell, S., Massonnet, F., and Tietsche,
893 S.: Improving predictions of Arctic sea ice extent, *Eos*, 96,
894 <https://doi.org/10.1029/2015EO031431>, 2015.

895 Stroeve, J., Hamilton, L. C., Bitz, C. M., and Blanchard-Wrigglesworth, E.: Predicting
896 September sea ice: Ensemble skill of the SEARCH Sea Ice Outlook 2008 – 2013,
897 *Geophys. Res. Lett.*, 41, 2411-2418, <https://doi.org/10.1002/2014GL059388>, 2014.

898 Tian-Kunze, X., Kaleschke, L., Maaß, N., Mäkynen, M., Serra, N., Drusch, M., and Krumpen,
899 T.: SMOS-derived thin sea ice thickness: Algorithm baseline, product specifications and
900 initial verification. *Cryosphere*, 8, 997-1018, <https://doi.org/10.5194/tc-8-997-2014>,
901 2014.

902 Tietsche, S., Day, J., Guemas, V., Hurlin, W., Keeley, S., Matei, D., et al.: Seasonal to
903 interannual Arctic sea ice predictability in current global climate models. *Geophysical*
904 *Research Letters*, 41, 1035–1043. <https://doi.org/10.1002/2013GL058755>, 2014.

905 Tsamados, M., Feltham, D. L., and Wilchinsky, A. V.: Impact of a new anisotropic rheology
906 on simulations of Arctic sea ice, *J. Geophys. Res. Oceans*, 118, 91–107,
907 [doi:10.1029/2012JC007990](https://doi.org/10.1029/2012JC007990), 2013.

908 Turner, A. K., and Hunke, E. C.: Impacts of a mushy-layer thermodynamic approach in global
909 sea-ice simulations using the CICE sea-ice model, *J. Geophys. Res. Oceans*, 120, 1253-
910 1275, [doi:10.1002/2014JC010358](https://doi.org/10.1002/2014JC010358), 2015.

911 Turner, A. K., Hunke, E. C., and Bitz, C. M.: Two modes of sea-ice gravity drainage: A
912 parameterization for large-scale modeling, *J. Geophys. Res.*, 118, 2279–2294,
913 [doi:10.1002/jgrc.20171](https://doi.org/10.1002/jgrc.20171), 2013.

914 Turner, J. S.: *Buoyancy Effects in Fluids*. Cambridge University Press, 368 pp. 1973.

915 Van den Dool, H.: *Empirical Methods in Short-Term Climate Prediction*, Oxford Univ. Press,
916 Oxford, U. K., 2006.

917 Wang, W., Chen, M., and Kumar, A.: Seasonal prediction of Arctic sea ice extent from a
918 coupled dynamical forecast system. *Monthly Weather Review*, 141(4), 1375–1394, 2013.

919 Warner, J. C., Armstrong, B., He, R., and Zambon, J.: Development of a coupled ocean–
920 atmosphere–wave–sediment transport (COAWST) modeling system. *Ocean Modell.* 35,
921 230–244, 2010.

922 Woodgate, R. A., Aagaard, K., and Weingartner, T. J.: A year in the physical oceanography of
923 the Chukchi Sea: Moored measurements from autumn 1990–1991. *Deep-Sea Res. II*, 52,
924 3116–3149, <https://doi.org/10.1016/j.dsr2.2005.10.016>, 2005.

925 Wu, W., Lynch, A. H., and Rivers, A.: Estimating the Uncertainty in a Regional Climate Model
926 Related to Initial and Lateral Boundary Conditions, *Journal of Climate*, 18(7), 917–933,
927 2005.

928 Yang, C.-Y., Liu, J., and Xu, S.: Seasonal Arctic sea ice prediction using a newly developed
929 fully coupled regional model with the assimilation of satellite sea ice observations.
930 *Journal of Advances in Modeling Earth Systems*, 12, e2019MS001938.
931 <https://doi.org/10.1029/2019MS001938>, 2020.

932 Zampieri, L., Goessling, H. F., and Jung, T.: Bright prospects for Arctic sea ice prediction on
933 subseasonal time scales. *Geophysical Research Letters*, 45, 9731– 9738.
934 <https://doi.org/10.1029/2018GL079394>, 2018.

935 Zhang, J. and Rothrock, D.: Modeling global sea ice with a thickness and enthalpy distribution
936 model in generalized curvilinear coordinates. *Mon. Wea. Rev.*, 131, 845–861, 2003.

937 Zhang, J., Lindsay, R., Steele, M., and Schweiger, A.: What drove the dramatic retreat of arctic
938 sea ice during summer 2007?, *Geophys. Res. Lett.*, 35, L11505,
939 [doi:10.1029/2008GL034005](https://doi.org/10.1029/2008GL034005), 2008.

940 Zhang, J., Schweiger, A., Steele, M., and Stern, H.: Sea ice floe size distribution in the marginal
941 ice zone: Theory and numerical experiments. *Journal of Geophysical Research: Oceans*,
942 120, 3484–3498. <https://doi.org/10.1002/2015JC010770>, 2015.

943 Zhang, J., Stern, H., Hwang, B., Schweiger, A., Steele, M., Stark, M., and Graber, H. C.:
944 Modeling the seasonal evolution of the Arctic sea ice floe size distribution. *Elementa:*
945 *Science of the Anthropocene*, 4(1), 126.
946 <https://doi.org/10.12952/journal.elementa.000126>, 2016.

947

948 **7. Tables**

949 Table 1 The summary of physic parameterizations used in the Y21_CRTL experiment

WRF physics	
Cumulus parameterization	Grell-Freitas (Freitas et al. 2018; improved from Y20)
Microphysics parameterization	Morrison 2-moment (Morrison et al. 2009; same as Y20)
Longwave radiation parameterization	CAM spectral band scheme (Collins et al. 2004; same as Y20)
Shortwave radiation parameterization	CAM spectral band scheme (Collins et al. 2004; same as Y20)
Boundary layer physics	MYNN2 (Nakanishi and Niino, 2006; improved from Y20)
Land surface physics	Unified Noah LSM (Chen and Dudhia, 2001; improved from Y20)
ROMS physics	
Tracer advection scheme	MPDATA (Smolarkiewicz, 2006; same as Y20)
Tracer vertical mixing scheme	GLS (Umlauf and Burchard, 2003; same as Y20)

Bottom drag scheme	Quadratic bottom friction (QDRAG; (same as Y20)
CICE physics	
Ice dynamics	EVP (Hunke and Dukowicz, 1997; improved from Y20)
Ice thermodynamics	Bitz and Lipscomb (1999; same as Y20)
Shortwave albedo	Delta-Eddington (Briegleb and Light, 2007; same as Y20)

950

951

952 Table 2 The summary of the prediction experiments and details of experiment designs.

953 Note: All experiments use the CFS operational forecasts as initial and boundary conditions; VT:

954 vertical transformation function; VS: vertical stretching function; SH94: stretching function of

955 Song and Haidvogel (1994); S10: stretching function of Shchepetkin (2010).

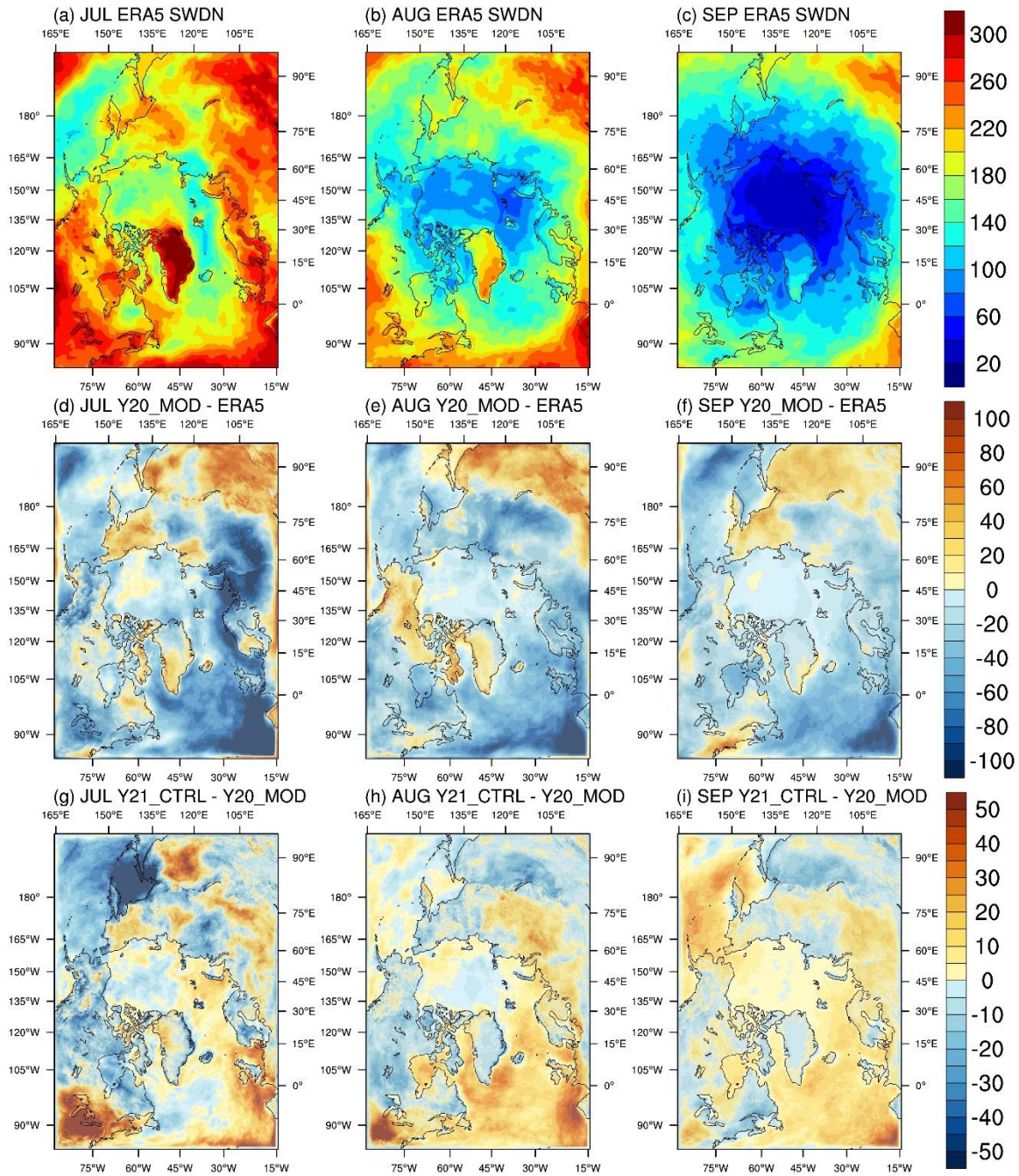
Experiment	Physics	Assimilation	ROMS vertical coordinate	Simulation period
Y20_MOD	Physics (old version) listed in Table 1	6 localization radii SSMIS SIC Simply-merged CryoSat- 2/SMOS SIT	VT 1 VS SH94 h_c 10m	2018.07.01- 2018.10.01
Y21_CTRL	Physics (new version) listed in Table 1	6 localization radii SSMIS SIC Simply-merged CryoSat- 2/SMOS SIT	VT 1 VS SH94 h_c 10m	2018.07.01- 2018.10.01
Y21_VT	Physics (new version) listed in Table 1	6 localization radii SSMIS SIC Simply-merged CryoSat- 2/SMOS SIT	VT 2 VS S10 h_c 300m	2018.07.01- 2018.10.01
Y21_RP	Advection: U3H/C4V	6 localization radii	VT 2	2018.07.01-

		SSMIS SIC	VS S10	2018.10.01
		Simply-merged CryoSat-2/SMOS SIT	h_c 300m	
Y21_MUSHY	Same physics as Y21_RP	6 localization radii	VT 2	2018.07.01-
		SSMIS SIC	VS S10	2018.10.01
	CICE: Mushy layer thermodynamics	Simply-merged CryoSat-2/SMOS SIT	h_c 300m	
Y21_SIT	Same physics as Y21_RP	6 localization radii	VT 2	2018.07.01-
		SSMIS SIC	VS S10	2018.10.01
		OI-merged CryoSat-2/SMOS SIT	h_c 300m	
Y21_EXT-7	Same physics as Y21_RP	6 localization radii	VT 2	2018.07.01-
		SSMIS SIC	VS S10	2019.01.31
		OI-merged CryoSat-2/SMOS SIT	h_c 300m	
Y21_MAR-7	Same physics as Y21_RP	6 localization radii	VT 2	2018.03.01-
		SSMIS SIC	VS S10	2018.09.30
		OI-merged CryoSat-2/SMOS SIT	h_c 300m	

956

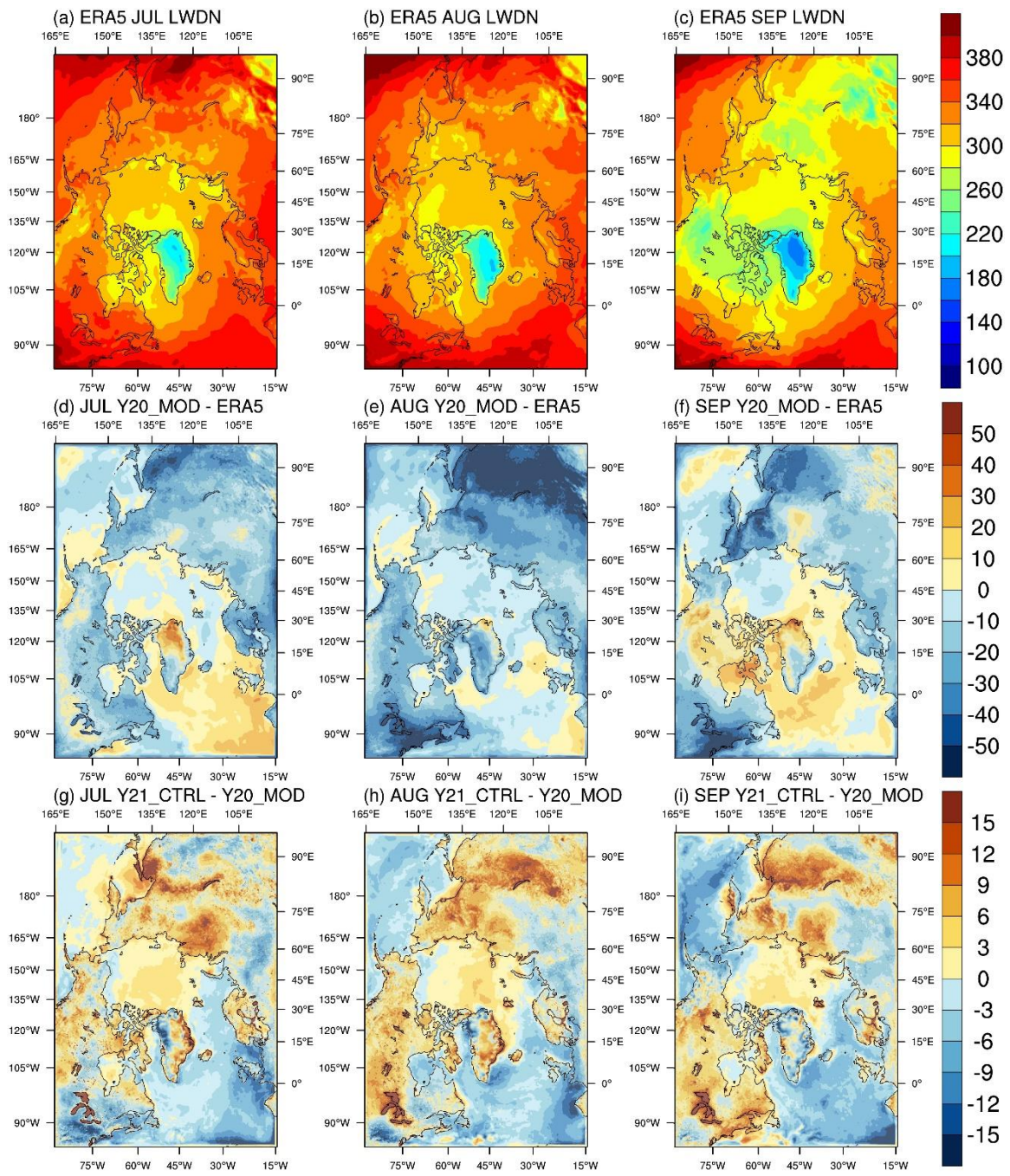
957

958 **8. Figures**



959
 960 Figure 1 ERA5 monthly mean of downward shortwave radiation at the surface for (a) July, (b)
 961 August, and (c) September, the difference between Y20_MOD and ERA5 for (d) July, (e)
 962 August, (f) September, and the difference between Y21_CTRL and Y20_MOD for (g) July, (h)
 963 August, and (i) September.

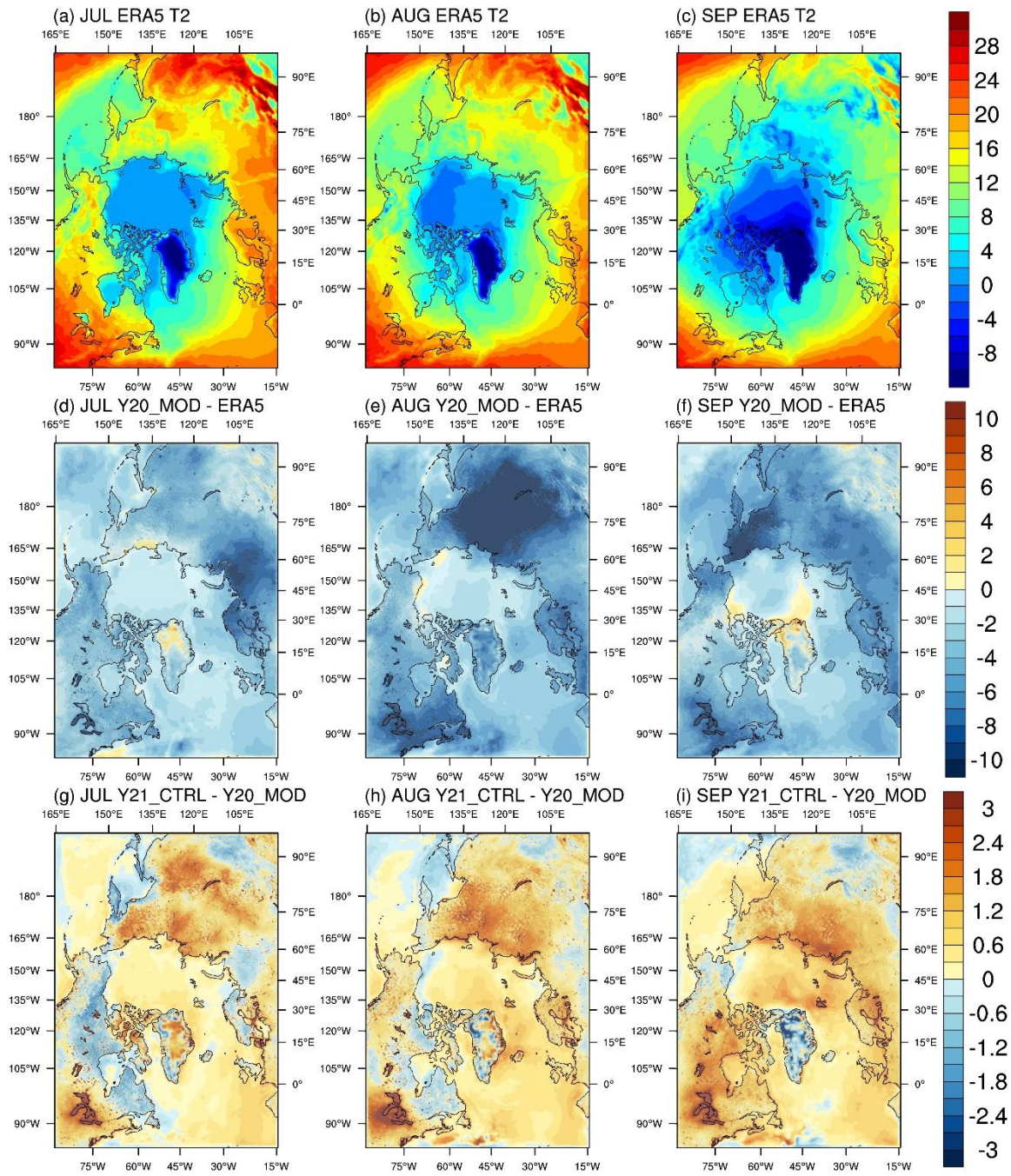
964



965

966 Figure 2 Same as Figure 1, but for downward thermal radiation at the surface.

967

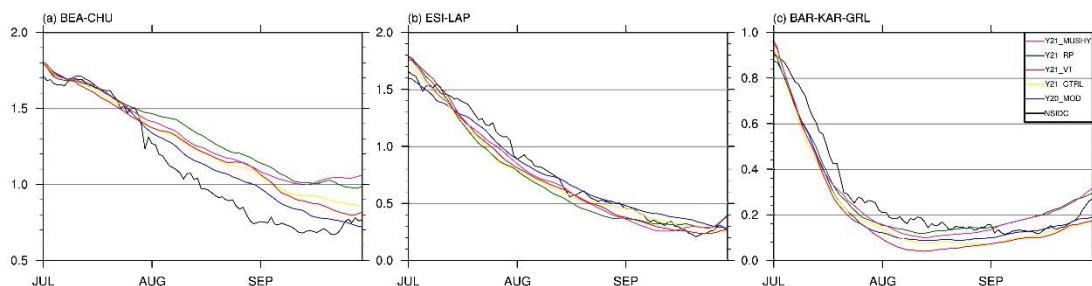
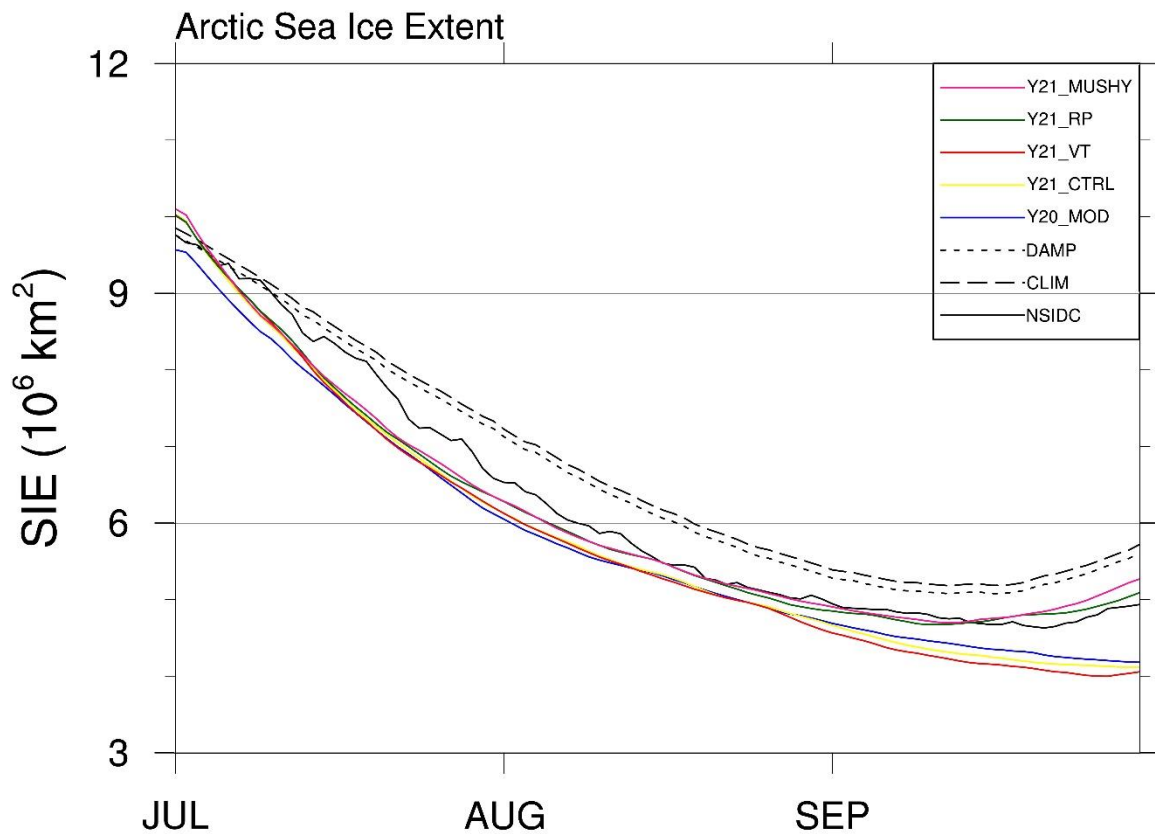


968

969 Figure 3 Same as Figure 1, but for near-surface air temperature.

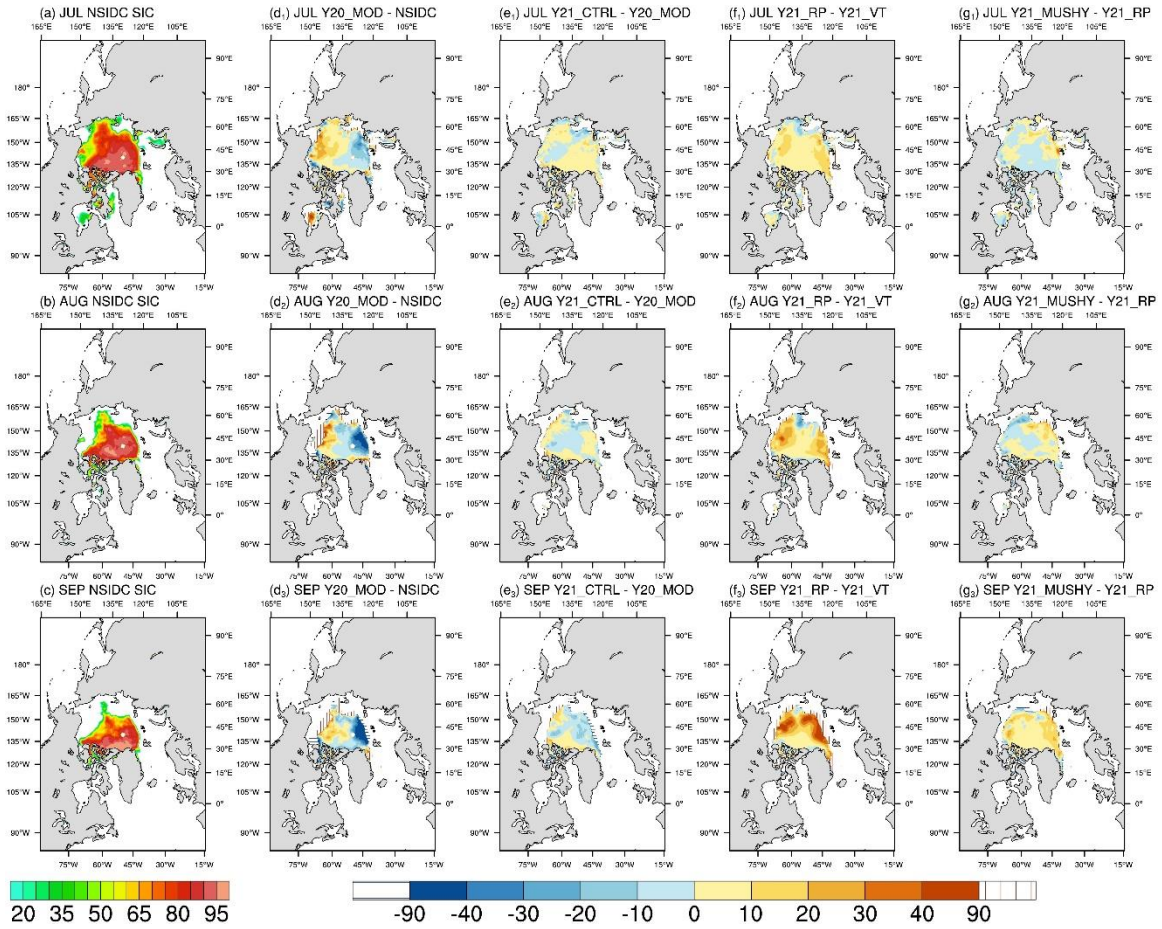
970

971



972

973 Figure 4 Top panel: Time-series of Arctic sea ice extent for the observations (black line) and
 974 the ensemble-mean of Y20_MOD (blue line), Y21_CTRL (yellow line), Y21_VT (red line),
 975 Y21_RP (green line), and Y21_MUSHY (pink line). Dashed and dotted lines are the
 976 climatology and the damped anomaly persistence predictions. Bottom panel: Time-series of
 977 the observed (black line) and the ensemble-mean of regional sea ice extents for Y20_MOD
 978 (blue line), Y21_CTRL (yellow line), Y21_VT (red line), Y21_RP (green line), and
 979 Y21_MUSHY (pink line) for (a) Beaufort-Chukchi Seas, (b) East Siberian-Laptev Seas, and
 980 (c) Barents-Kara-Greenland Seas.



981

982

983

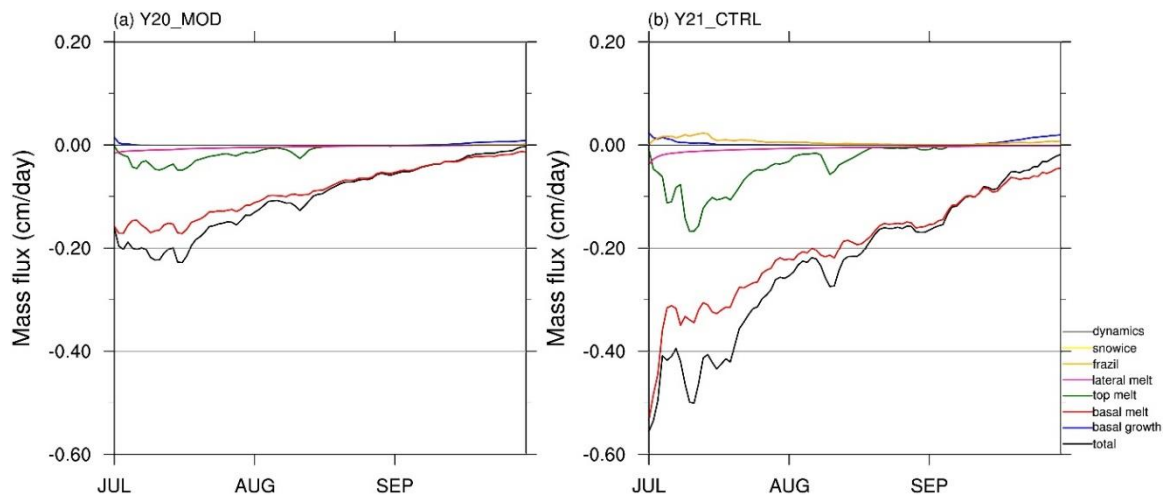
984

985

986

Figure 5 Monthly mean of sea ice concentration for (a) July, (b) August, (c) September of the NSIDC observations, and the difference between the all prediction experiments and the observations for (d₁-g₁) July, (d₂-g₂) August, (d₃-g₃) September. Vertical/horizontal-line areas represent the difference of ice edge location (15% concentration).

987

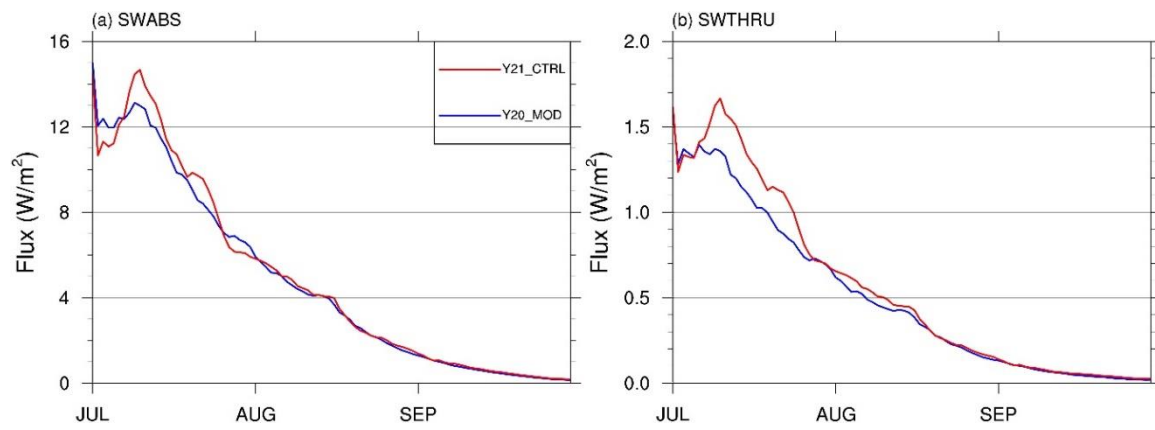


988

989 Figure 6 Time-series of sea ice mass budget terms for (a) Y20_MOD and (b) Y21_CTRL.

990

991



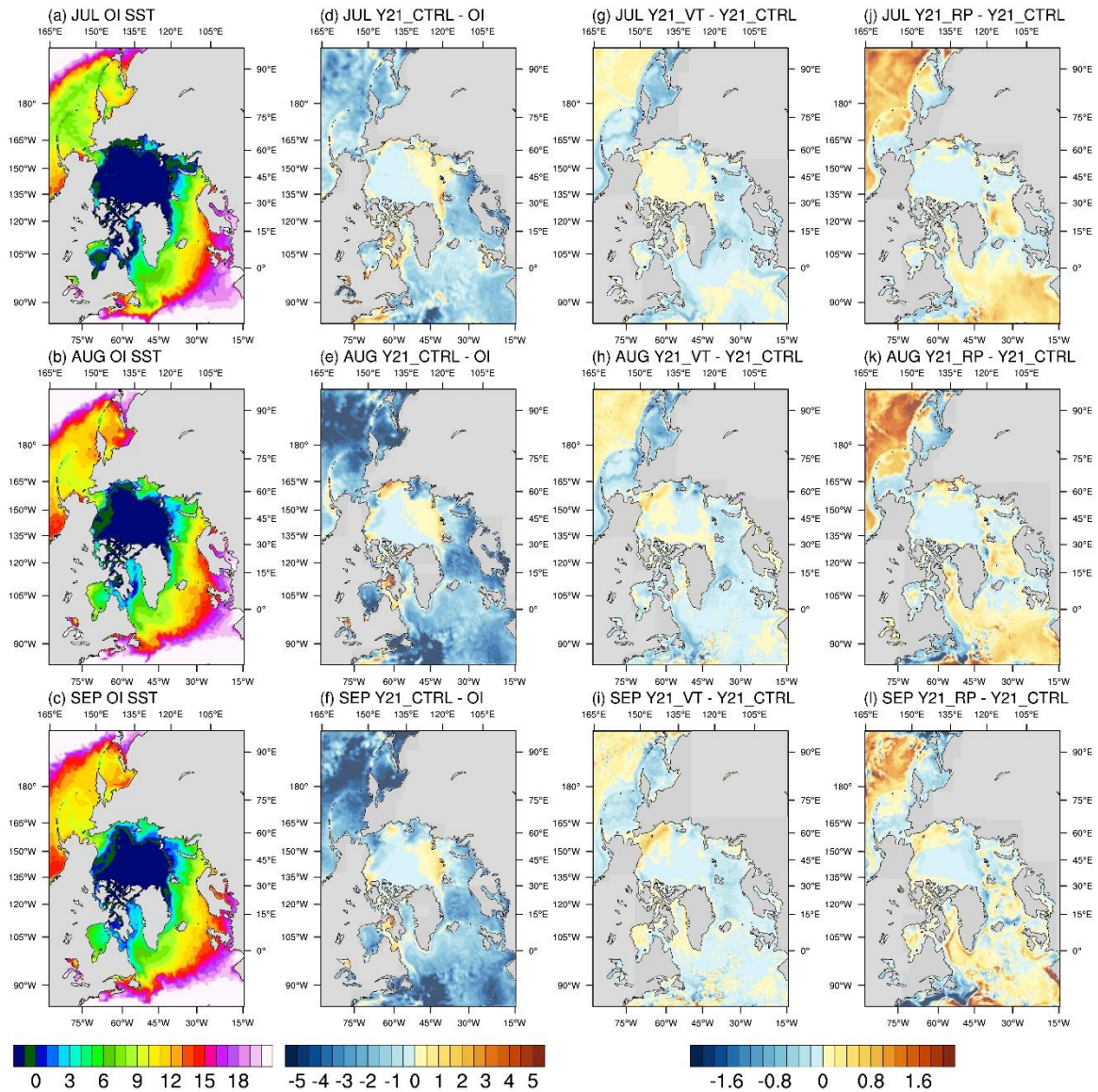
992

993 Figure 7 Time-series of (a) shortwave radiation absorbed by ice surface, and (b) penetrating

994 shortwave radiation to the upper ocean averaged over ice-covered grid cells for Y20_MOD

995 (blue line) and Y21_CTRL (red line).

996



997

998 Figure 8 First column: monthly mean of sea surface temperature for (a) July, (b) August, (c)

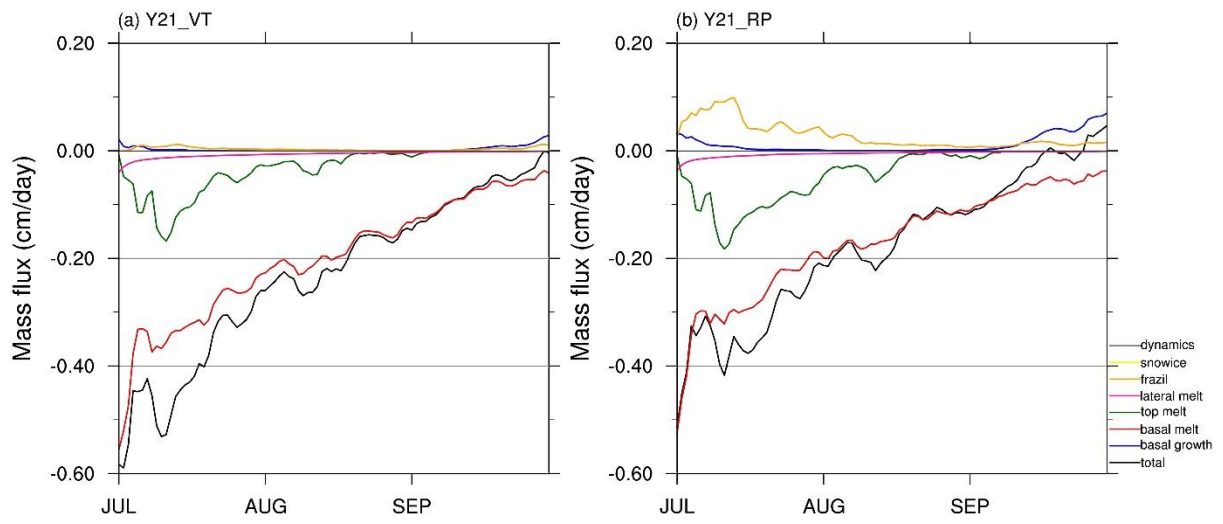
999 September of the OI SST. Second column: the difference between Y21_CTRL and the OI SST

1000 for (d) July, (e) August, (f) September. Right panel: Monthly mean of sea surface temperature

1001 difference between Y21_VT/Y21_RP and Y21_CTRL for (g) July, (h) August, (i) September

1002 of Y21_VT, (j) July, (k) August, and (l) September of Y21_RP.

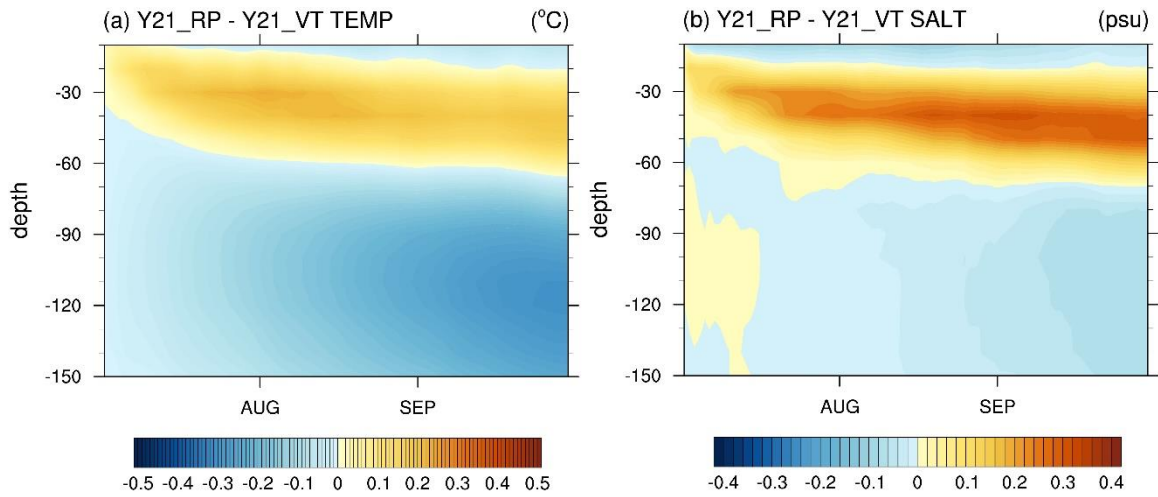
1003



1004

1005 Figure 9 Same as Figure 6, but for (a) Y21_VT, and (b) Y21_RP.

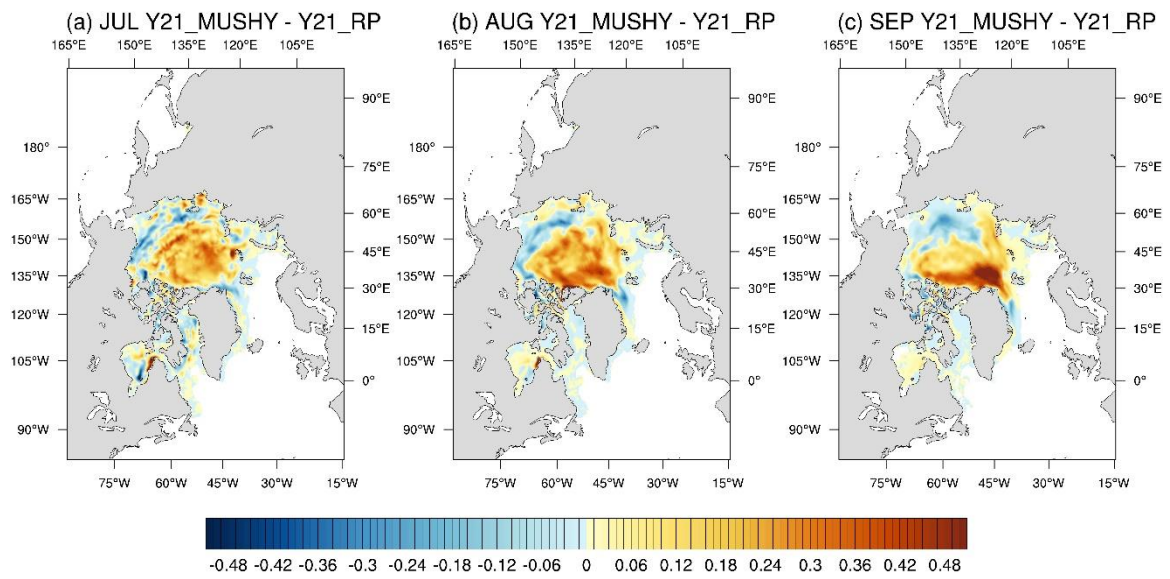
1006



1007

1008 Figure 10 (a) the average temperature profile of upper 150 m under ice-covered areas for the
1009 difference between Y21_RP and Y21_VT. (b) same as (a), but for the salinity profile.

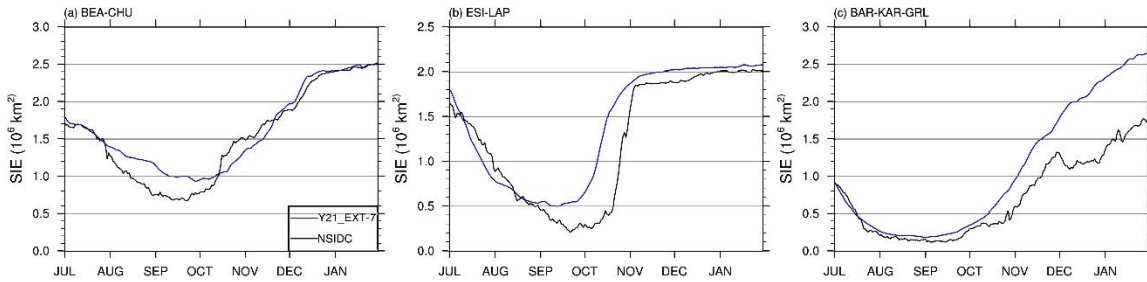
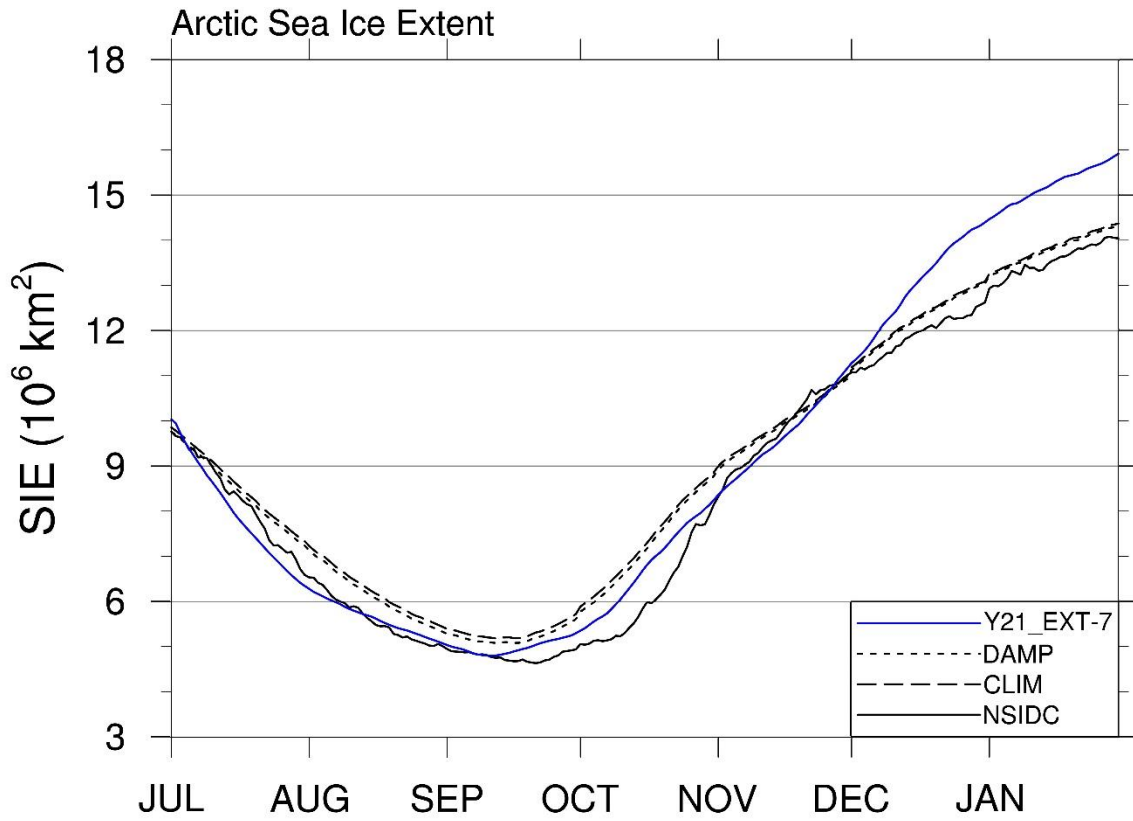
1010



1011

1012 Figure 11 Monthly mean of sea ice thickness difference between Y21_MUSHY and Y21_RP

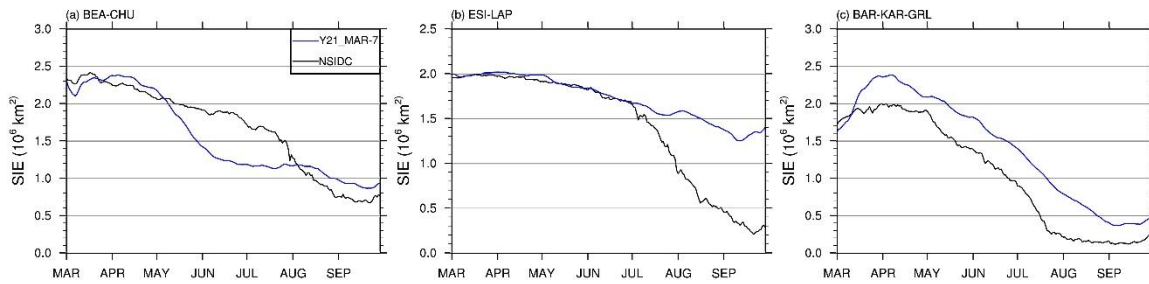
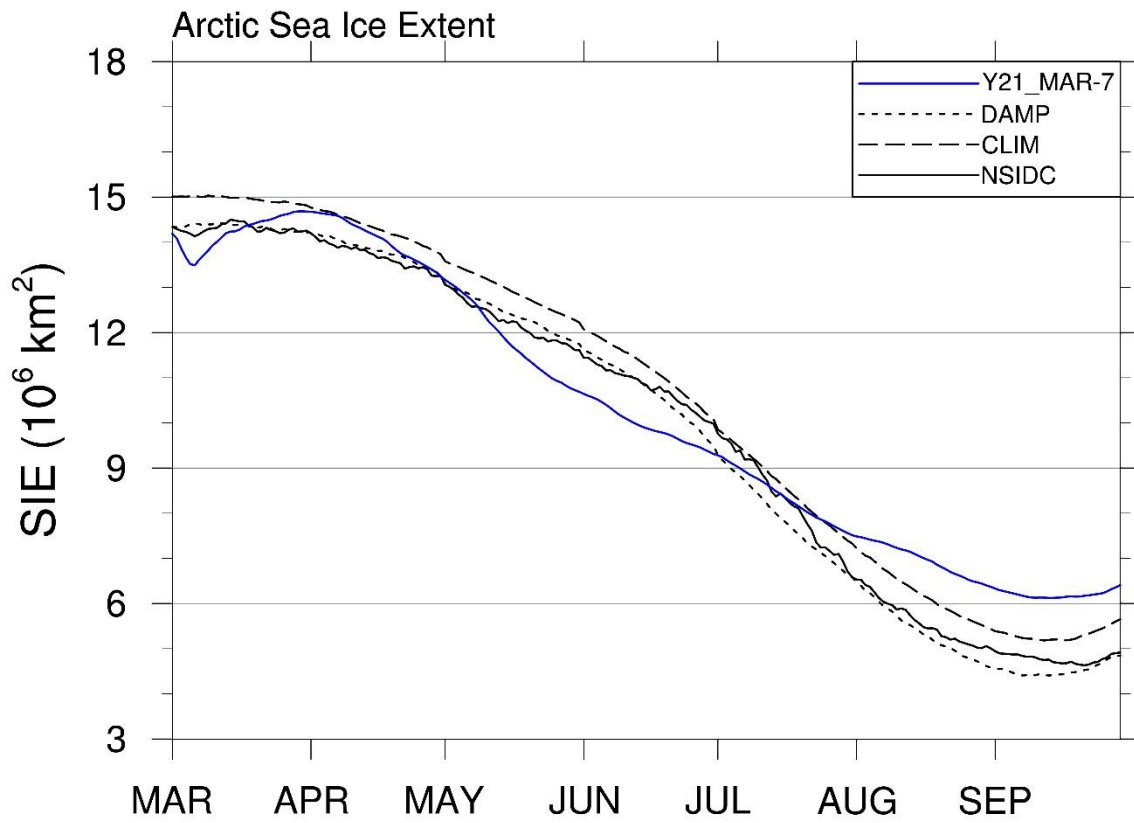
1013 for (a) July, (b) August, and (c) September.



1014

1015 Figure 12 Same as Figure 4, but for Y21_EXT-7.

1016



1017

1018 Figure 13 Same as Figure 4, bur for Y21_MAR-7.

1019